



HAL
open science

Non-linear dynamic modeling of ultrathin conducting polymer actuators including inertial effects

Ngoc Tan Nguyen, Yuta Dobashi, Caroline Soyer, Cedric Plesse, Giao T M Nguyen, Frederic Vidal, Eric Cattan, Sébastien Grondel, John D.W. Madden

► **To cite this version:**

Ngoc Tan Nguyen, Yuta Dobashi, Caroline Soyer, Cedric Plesse, Giao T M Nguyen, et al.. Non-linear dynamic modeling of ultrathin conducting polymer actuators including inertial effects. *Smart Materials and Structures*, 2018, 27 (11), pp.115032. 10.1088/1361-665X/aae456 . hal-02096105v1

HAL Id: hal-02096105

<https://uphf.hal.science/hal-02096105v1>

Submitted on 11 Apr 2019 (v1), last revised 22 May 2019 (v2)

HAL is a multi-disciplinary open access archive for the deposit and dissemination of scientific research documents, whether they are published or not. The documents may come from teaching and research institutions in France or abroad, or from public or private research centers.

L'archive ouverte pluridisciplinaire **HAL**, est destinée au dépôt et à la diffusion de documents scientifiques de niveau recherche, publiés ou non, émanant des établissements d'enseignement et de recherche français ou étrangers, des laboratoires publics ou privés.

Non-linear dynamic modeling of ultrathin conducting polymer actuators including inertial effects

Ngoc Tan Nguyen^{1,2}, Yuta Dobashi², Caroline Soyer¹, Cédric Plesse³, Giao T.M. Nguyen³,
Frédéric Vidal³, Eric Cattan¹, Sébastien Grondel^{1#}, John D.W. Madden²

1 Univ. Valenciennes, CNRS, Univ. Lille, Yncrea, Centrale Lille, UMR 8520 - IEMN, DOAE, F-59313
Valenciennes, France.

2 Advanced Materials and Process Engineering Laboratory, Electrical & Computer Engineering, University of
British Columbia, Vancouver, BC, V6T1Z4, Canada

3 LPPI, EA2528, Institut des Matériaux, Université de Cergy-Pontoise, 5 mail Gay Lussac, Neuville sur Oise, F-
95031 Cergy Cedex, France.

Corresponding Author/Email: sebastien.grondel@univ-valenciennes.fr

Abstract

Trilayer conducting polymer actuators are potential alternatives to piezoelectric and electrostatic actuators due to their large strain, and recently demonstrated operation at hundreds of Hertz. However, these actuators exhibit nonlinear electrical and mechanical properties as a function of their oxidation state, when operated over their full strain range, making it more challenging to accurately predict their mechanical behavior. In this paper, an analytical multi-physics model of the conducting polymer actuators is proposed to predict their non-linear dynamic mechanical behavior. To demonstrate the accuracy of the model, a trilayer actuator composed of a solid polymer electrolyte sandwiched between two poly(3,4-ethylenedioxythiophene) (PEDOT) electrodes was fabricated and characterized. This system consists of an electrical subsystem represented by an RC equivalent circuit, an electro-mechanical coupling matrix, and a mechanical subsystem described by using a rigid finite element method. The electrical conductivity and the volumetric capacitance, an empirical strain-to-charge ratio, and Young's modulus of the actuator as a function of the PEDOT electrode charge state were also implemented into the model, using measured values. The proposed model was represented using a Bond Graph formalism. The concordance between the

1 simulations and the measurements confirmed the accuracy of the model in predicting the non-
2 linear dynamic electrical and mechanical response of the actuators. In addition, the information
3 extracted from the model also provided an insight into the critical parameters of the actuators
4 and how they affect the actuator efficiency, as well as the energy distribution including
5 dissipated, stored, and transferred energy. These are the key parameters for designing,
6 optimizing, and controlling the actuation behavior of a trilayer actuator.
7
8
9

10
11 Keywords: conducting polymer actuator, multi-physics model, rigid finite element method,
12 nonlinear displacement, Bond Graph representation, energy harvesting.
13
14
15

16 **1. Introduction**

17
18

19 Conducting polymer (CP) based actuators have received particular attention from researchers
20 in various domains as they can be used for a variety of applications such as CP driven textiles
21 [1], position controlled of micro injection systems [2], medical applications [3-5], steerable
22 micro catheters [6], micro pumps driven by polypyrrole-based CP actuator [7, 8], micro
23 autofocus lens actuator [9], and micro patterning actuators [10-14], for example. Among the
24 different types of CPs, poly(3,4-ethylenedioxythiophene) (PEDOT) based-actuators have
25 sparked a great deal of interest because of their highly reversible, fast-switching redox
26 processes [15]. In addition, they are lightweight and biocompatible, they have a high stress (~
27 10 MPa) and a high power/weight ratio [16], they produce significant strain (up to 1%), require
28 low operating voltages (typically < 3 V) [17] in solutions or in open air condition [18], can be
29 electronically controlled with a reasonable frequency response (> 50 Hz) [19, 20] and are
30 potentially suitable for microscale applications [14]. However, the fabrication process of these
31 actuators normally requires manual handling, which reduces the reproducibility and makes it
32 difficult to fabricate a very thin structures needed when for rapid responses. A new clean-room
33 compatible process, referred to as layer-by-layer [14, 21, 22], has recently been demonstrated.
34 This technique eliminates the need for manual handling and promises to make the fabrication
35 of CP actuators highly automated.
36
37
38
39
40
41
42
43
44
45
46
47
48

49 In order to exploit this new actuator, modeling is necessary to predict their mechanical behavior
50 and identify important parameters.
51

52
53 Previously, for poly(pyrrole)-based actuators, Madden [23] came up with an analytical model
54 based on the diffusive elastic metal phenomenon to describe the charging process. This was
55 further extended by Shoa [24] to apply to bending structures. This chemical model was linked
56 to mechanical deformation through an experimentally-derived strain-to-charge ratio – an
57 empirical constant relating injected ionic charge density to strain. Alici [25] also proposed an
58
59
60

1 analytical model in which he emphasizes the effects of the double layer interface between the
2 electrolyte and the polymer electrode and models it as a capacitor and a resistor.
3

4 These previous studies employed equivalent circuit models. Since ionic EAP actuators
5 inherently involve mechanical and electrical energy flow combined with the chemical domain,
6 a comprehensive model to explain the behavior of this actuator must include coupling between
7 these multiple energy domains. Bond Graph (BG) methodology is well suited to describing
8 coupled domains [26, 27]. It allows easy access to the magnitudes of energy transformed (e.g.
9 between electrical and mechanical energy), stored power, and dissipated power inside these
10 actuators. BG language has shown its flexibility in working with different energy domains as
11 well as its feasibility for describing interactions between systems. These characteristics provide
12 an approach for designing actuators and further, designing of complete actuated robots, while
13 retaining the physical structure of the model [28]. Few studies investigate modeling CP
14 actuators using a BG. Byung-Ju Yi focused on the description of ions diffusion and chemical
15 reaction in separator and electrode layers of chemico-electro-mechanical coupling in trilayer
16 CP actuators using BGs, however the model was not verified by experiments [29]. Nishida
17 developed a more complex model on IPMCs type using a distributed port-Hamiltonian [28],
18 while Bowers built a BG model of bilayer actuators operating in electrolyte [30]. Recently,
19 Bentefrit [31] presented a finite-difference BG model of a trilayer actuator. However, this model
20 focuses on linear behavior, i.e. that it can only predict the mechanical displacement of the
21 actuator when the applied voltage is relatively small.
22
23
24
25
26
27
28
29
30
31
32
33
34
35

36 In this paper, the first goal is to build a non-linear dynamic model to predict the mechanical
37 behavior of ultrathin trilayer actuators. The non-linear mechanical behavior of these trilayer
38 actuators stems from changes that occur as the voltage is increased [32-34]. During operation,
39 oxidation in one PEDOT electrode layer and reduction in the other electrode, accompanied by
40 a drop in potential along the length of the electrodes, are observed. These changes in state
41 modify the electrical, coupling, and mechanical properties.
42
43
44
45
46

47 A number of investigations have been conducted on the non-linear properties, highlighting that
48 their inclusion significantly improves the predictive properties of models [32, 35-37]. In these
49 models, the mechanical inertial effects were excluded. Here, non-linearities are characterized
50 and included to describe the response of PEDOT electrodes; mechanical inertial effects are also
51 incorporated.
52
53
54
55

56 The second goal was the implementation of oxidation state dependent parameters into the
57 proposed model. The non-linear properties, including electrical conductivity, volumetric
58 capacitance of the PEDOT-based electrodes, and Young's modulus, were all characterized and
59
60

incorporated into the model. In addition, a set of experiments was conducted to confirm the concordance with the simulation results with regard to the current output and the actuation. From the proposed model, an evaluation of the sensitivity of the actuator parameters helps improve understanding of actuator performance and its crucial properties.

2. Modeling trilayer actuators

In this section, a nonlinear model for trilayer actuators is proposed. The model includes an RC electrical sub-system, an empirical coupling ratio, and a mechanical model. The model parameters are then identified and characterized experimentally.

2.1 Word BG model of an EAP actuator

A schematic of a PEDOT-based trilayer actuator is depicted in Fig. 1a. In these actuators, application of a voltage between the top and bottom electronically conductive layers leads to charging and ion transfer across the middle separator layer. The ion transfer leads to swelling of one of the conducting layers and contraction of the other, resulting in bending of the sandwich structure up or down. The proposed model of this actuator consists of three subsystems: the electrical sub system, the electro-mechanical coupling, and the mechanical subsystem. The connections between these subsystems are shown in Fig. 1b and are represented by “half arrows” indicating the assumed instantaneous positive flow of energy.

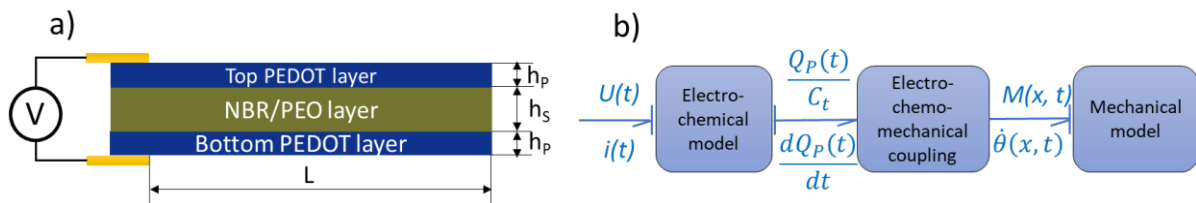


Fig. 1. a) Trilayer actuator, b) Trilayer actuator Words BG model.

The global system input is voltage, $U(t)$, whereas the outputs are current $i(t)$, beam angular velocity $\dot{\theta}(x, t)$, and beam curvature as a functions of position, x , along the trilayer, and time, t . The electrical model outputs the time and space charge variation of the actuator during the operation, $\frac{dQ_P(x, t)}{dt}$. Local charging is then related to strain and mechanical deformation through the electro-mechanical coupling system described below. The mechanical system is driven by the modal actuation moment $M(x, t)$ generated from coupling. In addition, each pair of input and output variables provides information about power transmission described as follows:

$$(voltage, \quad current) = (U(t), i(t)); \left(\frac{Q_P(x, t)}{C_P(t)}, \frac{dQ_P(x, t)}{dt} \right)$$

$$(\textit{moment}, \quad \textit{rotational angular velocity}) = (M(x, t), \dot{\theta}(x, t))$$

2.2 BG model of EAP actuators

Once the “Word BG” is obtained, the BG model describing each subsystem can be derived. A BG representation is composed of basic elements associated with ports: I and C are used for kinetic and potential energy storage, R for energy dissipation, ports Se and Sf as sources of effort (e.g. force and voltage) and flow (e.g. velocity and current).

2.2.1 Electrochemical model

An ultrathin trilayer configuration operating in air [38] is studied here. In this configuration, a solid polymer electrolyte (SPE), made of nitrile butadiene rubber (NBR) / poly(ethylene oxide) (PEO), accommodates cations 1-Ethyl-3-methylimidazolium (EMIm^+) and anions bis(fluorosulfonyl)imide (TFSI) and is sandwiched between two PEDOT containing CP electrodes. When an excitation voltage is applied between the two electrodes, the positive potential extracts electrons (oxidation process) from the one PEDOT electrode [39]. Cations leave the electrode to balance charge. At the other electrode, cations are injected by diffusion-like process into the CP layer neutralize the reduced polymer backbone [40, 41]. In addition, a voltage drop is observed along the trilayer due to the existence of the electrical resistance along the length of the PEDOT electrodes.

An RC equivalent circuit was proposed to explain the diffusion through the electrode thickness and the electrical resistance of PEDOT was added along the length of the electrodes, leading to a 2D transmission line model of a trilayer actuator [23, 24] (Fig. 2a). The diffusion line is described by capacitors C_{ij} , $i = 1, 3$, $j = 1, \dots, m$, and R_{ij} is the ionic resistance of the electrode layer. R_{1ie} , R_{3ie} are the electrical resistances along the length of the PEDOT electrodes. R_{sj} is the ionic resistance of the SPE layer, R_{short} is the possible short circuit resistance between the 1st and 3rd (electrode) layers, and C_{dli} is the double layer capacitance formed at the interface between the PEDOT electrodes and the SPE layer. The model can be simplified substantially because not all rate limiting factors are significant, in part since the ratio between the thickness and the length of the electrodes is small ($<1/10^3$). The magnitudes of these factors – the polymer charging time constant along the length, the diffusion time through the thickness of the electrodes, the double layer charging time, and the ionic transport through the SPE layer – are now estimated to determine which factors dominate. Estimates are based on time constants that are the product of a resistance and an effective capacitance [42]. The more important factors are selected and the 2D transmission line model is simplified, with a small effect on the accuracy. These rate limiting factors are calculated for a beam having a typical geometry of *length* (L) \times

width (b) \times total thickness (h) = 5 mm \times 1 mm \times 0.017 mm in the electrolyte swollen state, and thicknesses of a PEDOT electrode: $h_P = 3.5 \mu\text{m}$ and of SPE layer $h_S = 10 \mu\text{m}$.

The double layer charging time constant is determined by:

$$\tau_{dl} = R_S \times C_{dl} = \frac{h_S}{\sigma_S \times b \times L} b \times L \times C_A = \frac{10^{-5} \text{m} \times 0.2 \text{F/m}^2}{(0.038 \text{S/m})} = 53 \mu\text{s}, \quad (1)$$

where R_S and h_S are the resistance and the thickness of the SPE layer, respectively, b is the width of the actuator, L is the length of the actuator, C_A (F/m^2) is the double layer capacitance per area [43], and σ_S (S/m) is the ionic conductivity of the SPE layer which is characterized in section 2.4.

‘Effective diffusion time through electrodes’ thickness is calculated using the following formula:

$$\tau_D = \frac{h_P^2}{D} = \frac{(3.5 \times 10^{-6} \text{m})^2 \times (52 \times 10^6 \text{F/m}^3)}{0.025 \text{S/m}} = 0.0073 \text{ s}, \quad (2)$$

where h_P is the thickness, and D is the effective diffusion coefficient which is determined by σ_i (S/m), the ionic conductivity, divided by C_V (F/m^3), the volumetric capacitance of the electrode (the values of σ_i and C_V are referred to section 2.4), in the common case that it is the ionic resistance that limits the charging rate [23].

The resistance to ion transport through the SPE layer R_S is another rate limiting factor to be considered:

$$\tau_S = R_S \times C = \frac{h_S}{\sigma_S \times b \times L} \frac{C_V \times L \times b \times h_P}{2} = \frac{(10^{-5} \text{m}) 52 \times 10^6 \text{F/m}^3 (3.5 \times 10^{-6} \text{m})}{2 \times (0.038 \text{S/m})} = 0.0240 \text{ s}, \quad (3)$$

where the factor of “two” represents for two capacitors in series.

The polymer charge time constant resulting from the electronic resistance along the length of the electrodes is:

$$\tau_L = R_P \times C_V \times L \times b \times h_P = \frac{L}{\sigma_e h_P b} C_V \times L \times b \times h_P = \frac{(5 \times 10^{-3} \text{m})^2 52 \times 10^6 \text{F/m}^3}{2500 \text{S/m}} = 0.52 \text{ s}, \quad (4)$$

where R_P is the electrical resistance, V_P is the volume of the PEDOT electrode, σ_e is the PEDOT electrical conductivity (refer to section 2.4).

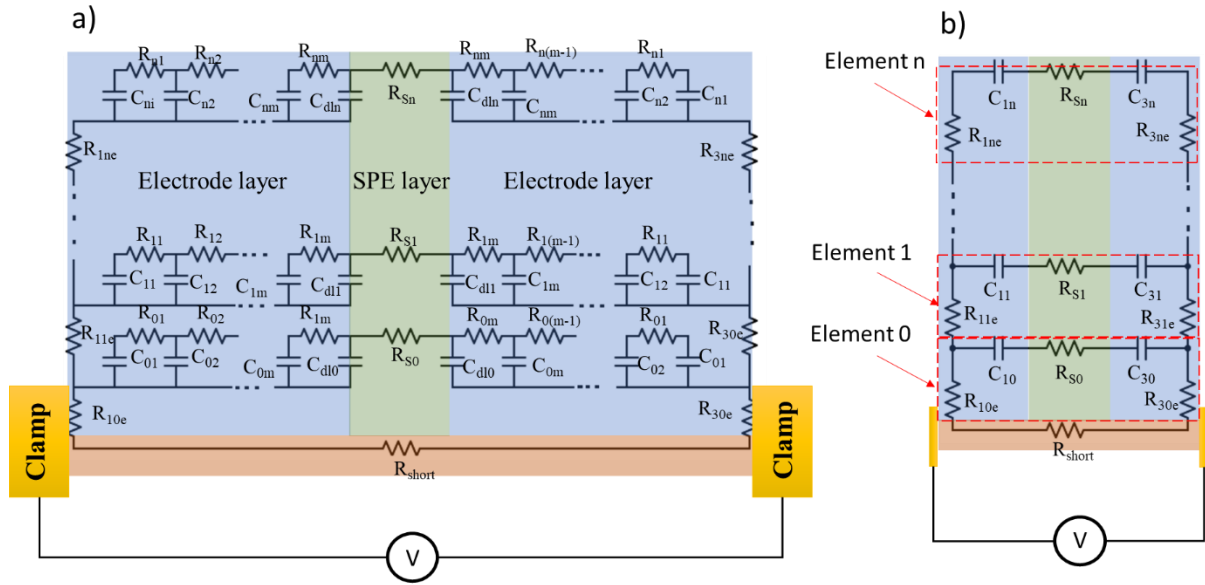


Fig.2. a) 2D diffusion line across the thickness and the length of a trilayer actuator, b) Simplified electrochemical model of the trilayer actuator.

As can be seen from four values above, the polymer charge time constant (0.52 s) and the resistance to ion transport through the SPE layer (0.024 s) play an important role in comparison to the diffusion time through the thickness (0.0073 s) and the double layer charging time constant (53 μ s). The 2D transmission line model shown in Fig. 2a can then be simplified to the 1D transmission line shown in Fig. 2b. The investigated trilayer actuator is divided into $n + 1$ elements corresponding to the space discretization.

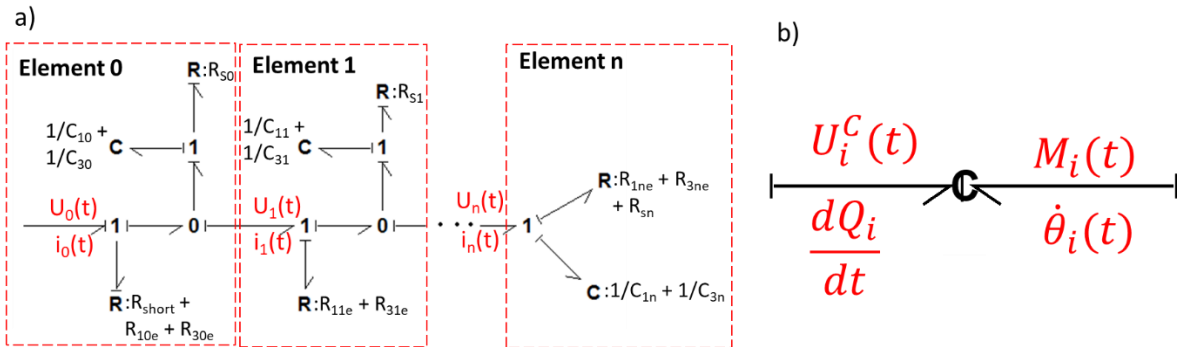


Fig. 3. a) BG representation of the electrochemical model, b) Coupling between the electrochemical subsystem and the mechanical subsystem.

The BG representation shown in the Fig. 3a. is used to describe the electrochemical model. Resistance and capacitance are indicated by the one-port R-elements and the one-port C-elements in the electrochemical system, respectively. The one-port C elements are shown for simplicity, - but in the full electromechanical model these are two-port \mathbb{C} -elements in which the charge state of the capacitor is coupled to the stress-strain state of the. As defined in all BG models, 0-junctions behave such that all the voltage values are equal across the bonds, and total current values in and out of the junction are equal zero. In the 1-junctions, the current is the

same through each bond and the sum of voltages is equal to zero. These are equivalent to parallel (0) and series (1) electrical circuit configurations.

2.2.2 Electro-mechanical coupling

BG language is especially advantageous for modeling the coupled electrochemical -mechanical effects. The electrochemical-mechanical coupling effects are represented by two-port \mathbb{C} -elements in BG. Trilayer bending strain results from both ion insertion and external forces applied to the polymer [44]. Accordingly, a two-port \mathbb{C} -element in this situation must have the ability to describe both energy transfer between different domains and energy storage in the electrodes. In Fig. 3b, the electro-mechanical coupling effect is depicted by a two-port \mathbb{C} -element with current dQ_i/dt and total moment M_i (including an external mechanical moment and a moment generated by an input current) implemented on both sides. Based on the relationship between total moment M_i and charge per volume ρ [44], the coupling matrix of a 2×2 element is established as follows:

$$\begin{bmatrix} U_i^C \\ M_i \end{bmatrix} = \begin{bmatrix} \frac{1}{C_i} & 0 \\ \frac{\alpha E_P (h_S + h_P)}{2L_i} & \frac{2b \sin(2\theta_i)}{3L_i \theta_i} E_P \left(\frac{h_S}{2}\right)^3 \left[\left(1 + \frac{2h_P}{h_S}\right)^3 - 1 + \frac{E_S}{E_P} \right] \end{bmatrix} \begin{bmatrix} Q_i \\ \theta_i \end{bmatrix}, \quad (5)$$

where U_i^C is the total voltage applied to the capacitor on the electrical side, α is an empirical strain-to-charge ratio [45], E_P Young's modulus of the electrode layer, and θ_i is the rotational angle of the i^{th} element relative to the direction of $(i-1)^{\text{th}}$ element. L_i is the length of element i and b is the width of the beam. In this coupling matrix, the bottom left element describes the effect of the strain-to-charge ratio on output moment, while the bottom right element relates the beam bending angle to the output moment, in which has been derived from the equations [44]:

$$F = \frac{E_P \alpha \rho}{L} b \left(\frac{h_S}{2}\right)^2 \left[\left(1 + \frac{2h_P}{h_S}\right)^2 - 1 \right] + \frac{2b E_P K}{3L} \left(\frac{h_S}{2}\right)^3 \left[\left(1 + \frac{2h_P}{h_S}\right)^3 - 1 + \frac{E_S}{E_P} \right],$$

where F is the total force produced by the trilayer actuator, $\rho = \frac{Q}{2Lbh_P}$ is the charge density, and $K = \frac{2w}{L^2 + w^2}$ is the curvature of the actuator. The factor of "0" on the top right of the coupling matrix represents the sensing coupling, in which a rotating angle, a displacement, or a stress are used as an input to induce an output voltage.

Furthermore, a nonlinear relationship between $M(L, t)$ and $Q(t)$ or $Q(t)/C_t(t)$ and $\theta(x, t)$ can be described through the coupling matrix, or in other words, the two-port \mathbb{C} -elements. The voltage $Q(t)/C_t(t)$ can also be decoupled from the moment $M(L, t)$ and vice versa.

2.2.3 Mechanical model

The generated moment from coupling effects is then applied to the trilayer actuator resulting in the bending. Since the ratio between thickness and length of the ionic EAP actuator is small $((2h_p + h_s)/L \ll 1)$, this actuator can be considered as a thin beam.

In addition, evidence of the large displacement of the trilayer actuator used in this study and shown in Fig. 13 suggests that a non-linear model should be developed to describe the mechanical system. Several beam modeling methods exist, such as, for a small displacement: the Euler-Bernoulli beam theory [46], the Timoshenko beam theory, and the Rayleigh-Ritz beam theory [47], and for a large displacement such as the Galerkin finite element method to solve second order non-linear differential equations [48], as well as the rigid finite element method (RFEM) [49]. RFEM allows us to take into account the non-linear dynamic mechanical behavior of the actuator easily, and to account for inertia [27, 50, 51]. Effects of mass have been left out of previous models since conducting polymer actuators have historically been slow. However the PEDOT-NBR/PEO trilayer presented in this work have been shown to be fast in their responses [19], so inclusion of inertial effects in the proposed model is important to predict the actuation at high operating frequencies.

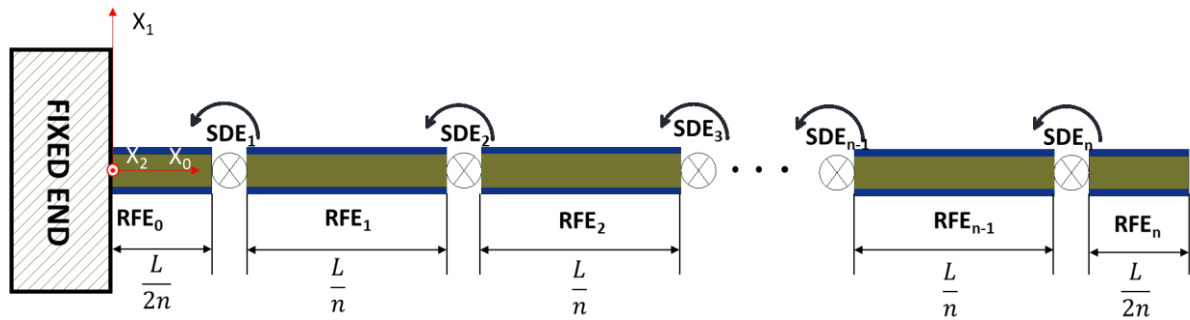


Fig. 4. Rigid Finite Element Model (RFEM) of a trilayer actuator, in which it is divided into $(n+1)$ rigid elements: from RFE_0 to RFE_n , the elements each have a mass and are linked by spring-dampers SDE_1 to SDE_n , shown in their initial positions.

So, if we consider RFEM, the actuator is divided into $(n + 1)$ rigid elements from RFE_0 to RFE_n , where the length of each element is calculated according to the following rule: $L_i = L/n$, $i = 1, \dots, n-1$ and $L_0 = L_n = L/2n$. Each element is rigid and has a mass. Consecutive elements link together by a torsional spring-damping element (SDE), which allows a rotation around its axis X_2 (perpendicular to X_0X_1 surface) (Fig. 4). The general Lagrange principle at each SDE is written as follows:

$$\frac{d}{dt} \left(\frac{\partial T}{\partial \dot{\theta}_i} \right) - \frac{\partial T}{\partial \theta_i} + \frac{\partial V}{\partial \theta_i} + \frac{\partial D}{\partial \dot{\theta}_i} = M_i \quad , \quad (6)$$

where $i = 1, \dots, n$, and T , V , and D are the kinetic energy, potential energy, and dissipation energy, respectively, of the system of $(n+1)$ elements. The terms in the equation are now described mathematically, following the treatment presented by Wittbrodt *et al.* [51].

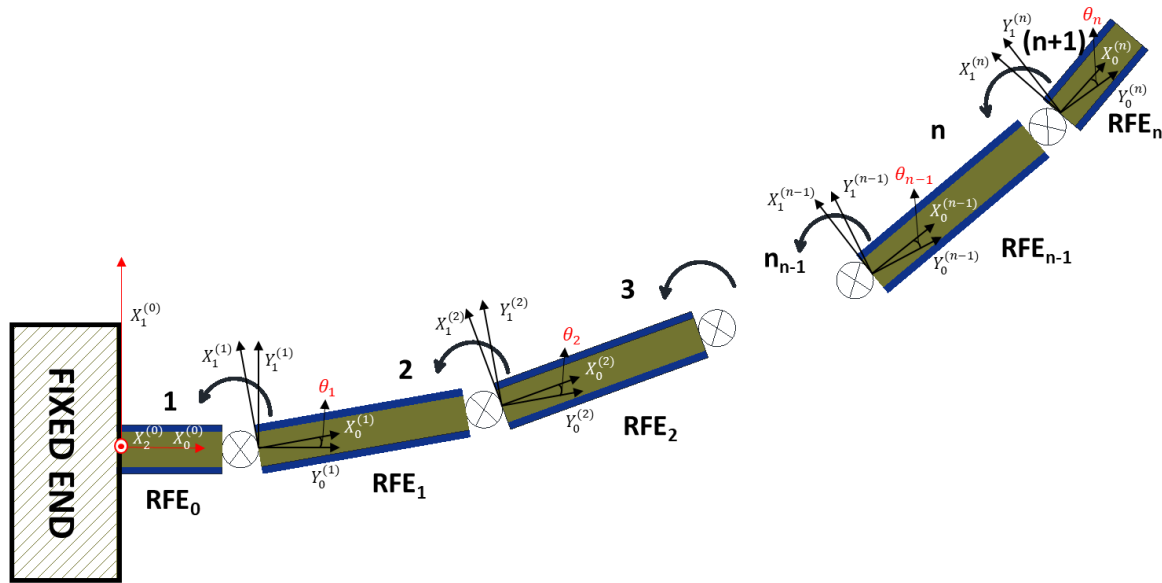


Fig. 5. Trilayer actuator in a bent state. The bending angle between the element $(i-1)$ and the element i is θ_i .

Considering a differential element dm_i on RFE_i , the kinetic energy of this element is:

$$dT_i = \frac{1}{2} \text{tr}\{\dot{r}_i \dot{r}_i^T\} dm_i, \quad (7)$$

where $r_i = [X_0^{(i)} \quad X_1^{(i)}]^T \cdot X_0^{(i)}$, and $X_1^{(i)}$ are the components of displacement in two axes of the i^{th} element, in the local coordinates, as depicted in Fig. 5. The total kinetic energy of the system is then:

$$T_i = \frac{1}{2} \int_{m_i} \text{tr}\{\dot{r}_i \dot{r}_i^T\} dm_i = \frac{1}{2} \text{tr}\{\dot{B}_i H_i \dot{B}_i^T\}, \quad (8)$$

$$\text{where pseudo-matrix } H_i = \int_{m_i} \dot{r}_i \dot{r}_i^T dm_i = \begin{bmatrix} m_i L_i^2 / 3 & 0 & m_i L_i / 2 \\ 0 & m_i h^2 / 12 & 0 \\ m_i L_i / 2 & 0 & m_i \end{bmatrix}, \quad (9)$$

m_i is the mass of the RFE_i , h is the thickness of the actuator, and L_i is the length of the RFE_i .

The matrix $B_i = \check{B}_1 \check{B}_2 \dots \check{B}_i$, enables the description of the total rotation of an element and its position as a function of time. Here, $\check{B}_i = \begin{bmatrix} \text{Cos } \theta_i & -\text{Sin } \theta_i & L_i \\ \text{Sin } \theta_i & \text{Cos } \theta_i & 0 \\ 0 & 0 & 1 \end{bmatrix}$, which represents the rotational matrix of the element the RFE_i , expressed in terms of angles, θ_i , relative to the previous beam segment RFE_{i-1} , and the length of each segment, L_i (Fig. 5).

Then the total kinetic energy of the system is obtained by the sum of T_i :

$$T = \sum_{i=1}^n T_i. \quad (10)$$

The total potential energy of the system is $V = \frac{1}{2} \sum_{i=1}^n k_i \theta_i^2$ (9), where $k_i = \frac{EI}{L_i}$, which is the stiffness of each RFE_i element [52].

The total dissipation energy is $D = \frac{1}{2} \sum_{i=1}^n c_i \dot{\theta}_i^2$ (10), where $c_i = \frac{\eta I}{L_i}$, η is the normal damping material constant, I is the inertial moment, and E is the Young's modulus of the actuator.

The external moment is determined by the electro-mechanical coupling established from equation (5).

The final Lagrange equation is obtained by inserting equations (8), (9), and (10) into (6).

In order to describe the Lagrange principle in a BG, the component $\frac{d}{dt} \left(\frac{\partial T}{\partial \dot{\theta}_i} \right)$ needs to be rewritten as the following chain:

$$\frac{d}{dt} \left(\frac{\partial T}{\partial \dot{\theta}_i} \right) = \sum_{j=1}^n \left[\frac{\partial}{\partial \theta_j} \left(\frac{\partial T}{\partial \dot{\theta}_i} \right) \frac{\partial \theta_j}{\partial t} + \frac{\partial}{\partial \dot{\theta}_j} \left(\frac{\partial T}{\partial \dot{\theta}_i} \right) \frac{\partial \dot{\theta}_j}{\partial t} \right], \quad (11)$$

and the component \dot{B}_i is described as:

$$\dot{B}_i = \frac{dB_i}{dt} = \sum_{j=1}^i \left[\frac{\partial B_i}{\partial \theta_j} \frac{\partial \theta_j}{\partial t} \right]. \quad (12)$$

This set of Lagrange equations can be rewritten in the following form:

$$\begin{aligned} \ddot{\theta}_1 &= f(\dot{\theta}_1, \dot{\theta}_2, \dots, \dot{\theta}_n, \theta_1, \theta_2, \dots, \theta_n, t) \\ \ddot{\theta}_2 &= f(\dot{\theta}_1, \dot{\theta}_2, \dots, \dot{\theta}_n, \theta_1, \theta_2, \dots, \theta_n, t), \\ &\vdots \\ \ddot{\theta}_n &= f(\dot{\theta}_1, \dot{\theta}_2, \dots, \dot{\theta}_n, \theta_1, \theta_2, \dots, \theta_n, t) \end{aligned} \quad (13)$$

or in a compact form:

$$I(\theta, \ddot{\theta}) \cdot \ddot{\theta} + R\dot{\theta} + C\theta + e(\theta, \dot{\theta}) = M. \quad (14)$$

In our case, since the actuator is initially curved, the initial condition can be provided by setting the vector of the rotational angles of the RFEs at the time $t = t_0$: $\theta(t_0) = [\theta_1(t_0) \ \theta_2(t_0) \ \dots \ \theta_n(t_0)]^T$. Assuming that the actuator is stationary at the time $t = t_0$: $\dot{\theta}(t_0) = [\dot{\theta}_1(t_0) \ \dot{\theta}_2(t_0) \ \dots \ \dot{\theta}_n(t_0)]^T = [0 \ 0 \ \dots \ 0]^T$. Finally, the results form a matrix of rotational angles at each SDE during the time span $t = t_0, \dots, t_m$, where time has been divided into m :

$$\begin{bmatrix} \theta(t_0) \\ \theta(t_1) \\ \vdots \\ \theta(t_m) \end{bmatrix} = \begin{bmatrix} \theta_1(t_0) & \theta_2(t_0) & \dots & \theta_n(t_0) \\ \theta_1(t_1) & \theta_2(t_1) & \dots & \theta_n(t_1) \\ \dots & \dots & \dots & \dots \\ \theta_1(t_m) & \theta_2(t_m) & \dots & \theta_n(t_m) \end{bmatrix}. \quad (16)$$

Knowing the rotational angles as a function of time, the position of the RFEs and the actuator shape can be easily derived.

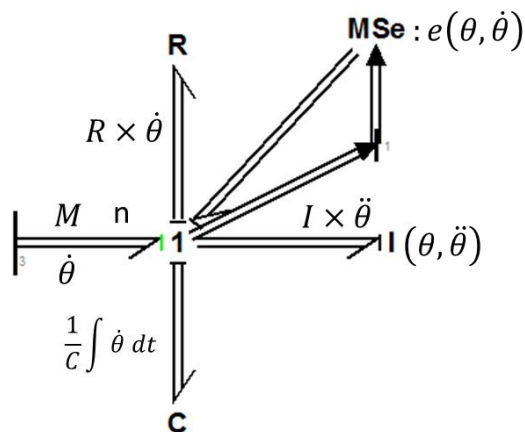


Fig. 6. Mechanical BG model.

Based on equation (14), the mechanical BG model is described as in Fig. 6. Here, the input power, represented by the applied moment, M , and the angular velocity $\dot{\theta}$, is divided among n-port R-elements, n-port C-elements, n-port I-elements, and a multiport source element MSe, which indicates the damping constant, the inverse of the spring constant, the mass, and non-linear dynamic rotation $e(\theta, \dot{\theta})$. The *multi-bond graph* notation (n bonds) is used here since it turns out to be a natural and concise way of representing the power behavior of macroscopic multiport systems.

2.3 The global BG model of the actuator

In previous sections, the electrochemical model, the electrochemical-mechanical coupling, and the mechanical model were established. To form the global model, the electrochemical model is combined with the electro-mechanical coupling in BG. The moment is exported from the coupling, and then transmitted into the mechanical model. For simplicity, the elements in the model are organized and divided into small subsystems as depicted in Fig. 7.

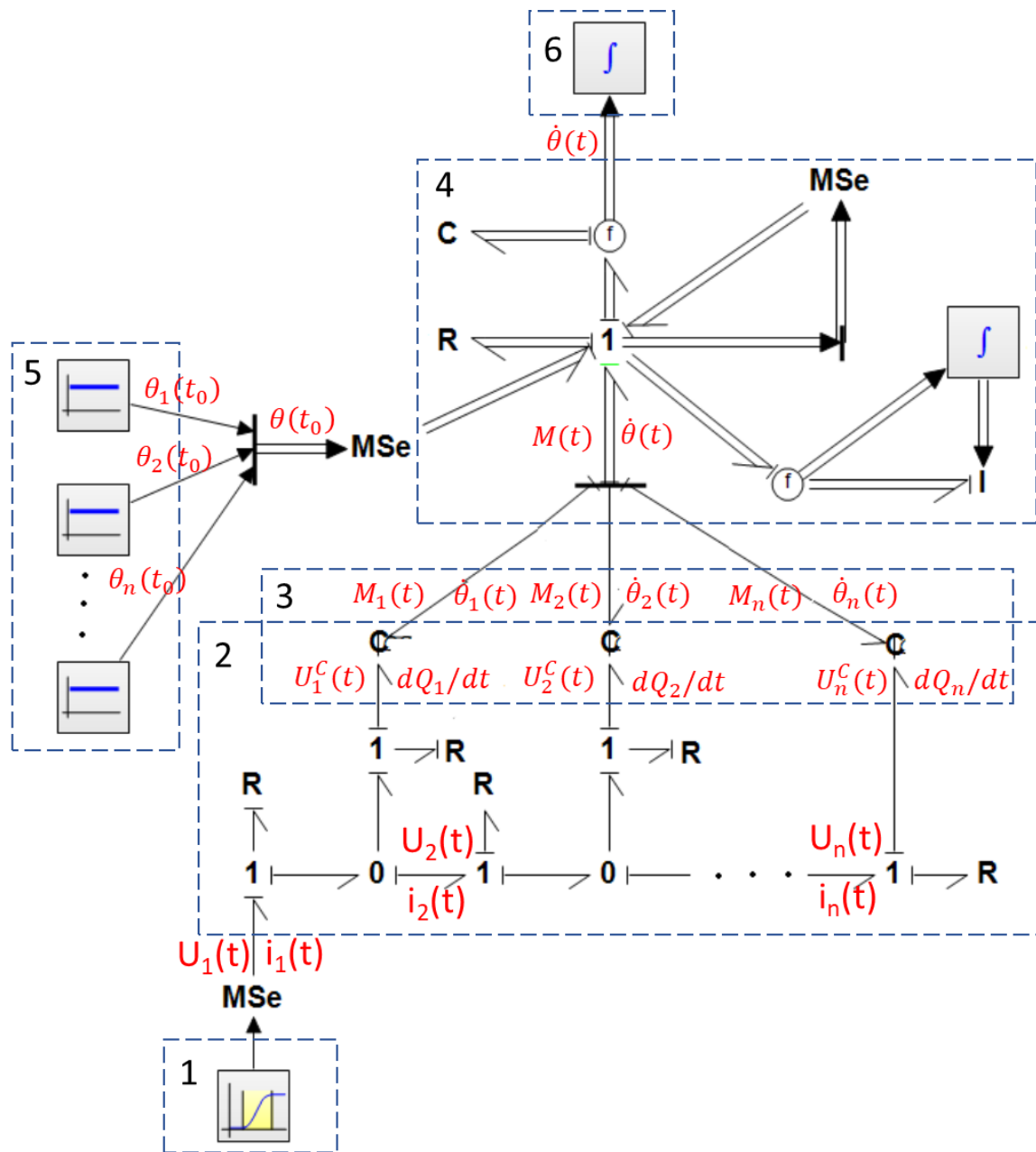


Fig. 7. CP actuator global model: 1. Voltage source, 2. Electrochemical model, 3. Coupling between electrochemical and mechanical part, 4. Mechanical model, 5. Boundary conditions: initial stress, 6. Displacement output.

It is worth noticing that the number of the RFE elements is $(n + 1)$ whereas the SDE elements is n . Theoretically, the higher the number of RFE elements is, the more precise the simulation will be in comparison with the analytical method but at the expense of computational time. A rough estimation has shown that the relative error is 1.14 % and 0.41 % at first resonant frequency [49] with respect to the analytical method solution when the number of RFE is 4 ($n = 3$) and 6 ($n = 5$), respectively. Within our proposed model, we have chosen two cases where $n = 3$ (3 SDEs) and $n = 5$ (5 SDEs) to investigate the accuracy of our model.

3. Characterization of trilayer parameters

In this section, the electrical, empirical coupling, and mechanical properties of the trilayer actuator, which are necessary for the proposed model, are characterized. The materials and the NBR/PEO, the bilayer, and the trilayer fabrication process were detailed in [38].

3.1 Electrochemical properties

A number of properties limit current and charging speed. Polymer ionic conductivity is one of these factors [53] (refer to equation 1, 2, 4), which in turn is a factor that can limit strain rate and bending speed of the trilayer actuator. The PEDOT ionic conductivity was determined using an Electrochemical Impedance Spectroscopy (EIS) measurement according to a procedure described previously [53, 54] (refer to supplementary information Fig. SIII). It has been shown that there is an asymmetry between the top and the bottom PEDOT electrodes in a trilayer actuator fabricated by vapor phase polymerization [38]. Therefore, a top bilayer (PEDOT electrode is polymerized on the top of NBR/PEO) and a bottom bilayer (PEDOT electrode is polymerized on a silicon wafer followed by a NBR/PEO layer) were investigated separately to find out the variation in PEDOT ionic conductivity. Before the measurement, an NBR/PEO membrane, as well as the top-coated bilayer and the bottom-coated bilayer samples (PEDOT coated NBR/PEO) were immersed into EMImTFSI for two weeks, to ensure a full uptake of ions. To separate the PEDOT ionic resistance from other sources of resistance such as NBR/PEO resistance and ionic liquid resistance, the thickness of specimens (Table 1) was increased during the fabrication process.

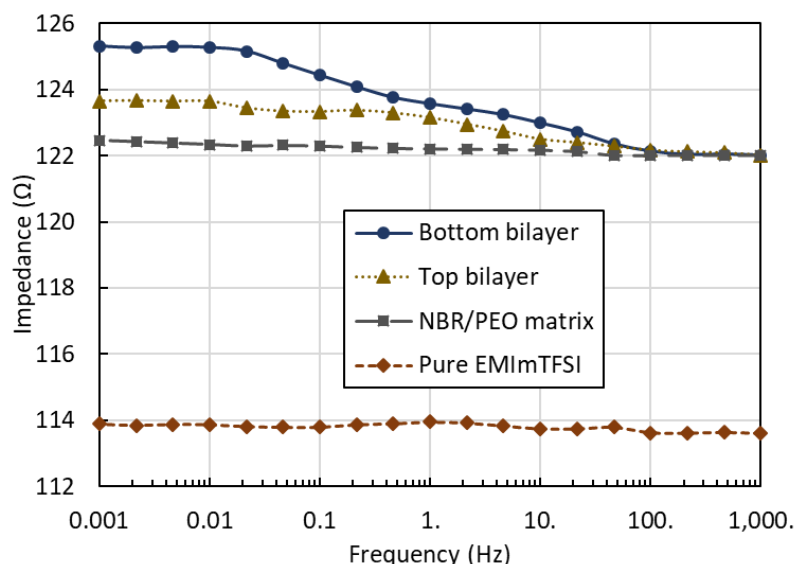


Fig. 8. Impedance values obtained from EIS measurements of a pure EMImTFSI, a top bilayer of NBR/PEO-PEDOT, a bottom bilayer of PEDOT-NBR/PEO, and a single NBR/PEO layer.

The EIS experimental results are shown in Fig. 8. At long times and low frequencies this impedance is dominated by the ionic resistance of the sample, and of the electrolyte between the sample and the tips of the cannulas. This ionic resistance may include either the PEDOT and the NBR/PEO ionic resistance in the case of a bilayer, or only the NBR/PEO ionic resistance for a single NBR/PEO layer. By contrast, at high frequency, a local potential drop occurs in the electrolyte and along the NBR/PEO thickness, as the electronic conductivity of the PEDOT layers shields these regions [53]. The ionic conductivity (σ) of the PEDOT and NBR/PEO layer is determined by:

$$\sigma = \frac{h}{R \times A},$$

where h is the thickness of either the PEDOT or the NBR/PEO layer (Table 1), and A is the sample surface area. Resistance, R , is calculated by a subtraction between NBR/PEO containing cell resistance and pure EMImTFSI resistance (Fig. 8) to estimate the resistance of the NBR/PEO alone. To find the ionic resistances of the PEDOT layers, the difference in resistance between low EIS frequency (0.001 Hz – representing the resistance of all layers) and high frequency (resistance at 1 kHz – representing the resistance of NBR/PEO plus EMImTFSI), for the same bilayer.

Table 1. Thickness in swollen state and ionic conductivity of the NBR/PEO alone, NBR/PEO top-coated with PEDOT, and bottom-coated with PEDOT

| | Thickness (swollen) (μm) | Ionic conductivity (S/m) |
|--------------------|---------------------------------------|--------------------------|
| NBR/PEO layer | 25.3 | 0.038 |
| Top PEDOT layer | 7.1 | 0.025 |
| Bottom PEDOT layer | 3.2 | 0.030 |

As can be seen in the Table 1, there is a slight difference between the ionic conductivity of the top and the bottom PEDOT electrodes indicating a small effect of the asymmetry on the ionic conductivity.

Researchers have demonstrated that the electronic conductivity of PEDOT depends on the potential applied [32, 55, 56]. In this work, the electrical conductivities of the thin PEDOT electrode layers have been characterized to explore their dependences on the potential applied. To measure the electrical conductivity as a function of oxidation state, a potential (versus Ag/AgCl reference electrode) was applied to both sides of a trilayer structure in solution (refer to the supplementary information Fig. SII2a). The dimensions of the specimen are *length* (L) \times *width* (b) \times *total thickness* (h) = 10 mm \times 3 mm \times 0.017 mm in swollen state, and the thicknesses of each of the layers are $h_P = 3.5 \mu\text{m}$ and $h_S = 10 \mu\text{m}$. Electrical conductivity was then measured

on the top and bottom surfaces of the trilayer structure using a four-line probe (refer to the supplementary information Fig. SII2b).

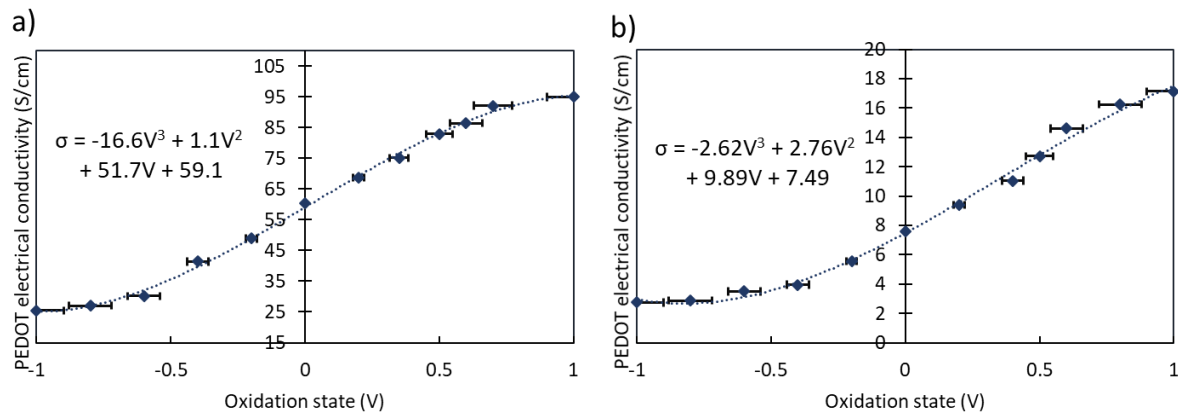


Fig. 9. PEDOT electrical conductivity: a) on the bottom PEDOT surface of the trilayer structure, b) on the top PEDOT surface of the trilayer structure

Fig. 9. shows the electrical conductivities of the bottom and the top PEDOT electrodes in a trilayer configuration. As expected [32, 56], the electrical conductivity drops markedly - by a factor of 4 (Fig. 9a) and 5 (Fig. 9b) in this case - as the PEDOT electrode approaches its reduced state. This change fits a third order function, which will later be used in the model. The electrical conductivity of the bottom PEDOT electrode is about eight times higher than that of the top PEDOT electrode, confirming the asymmetry of the top and the bottom electrodes. This asymmetry stems from the actuator fabrication process, which is based on the layer-by-layer method, where the bottom PEDOT layer in contact with a silicon wafer has the longer heat treatment period and the smoother surface, while the top PEDOT layer formed on the NBR/PEO surface is rougher and treated for a shorter period. Another contribution to this asymmetry is the bottom-up forming mechanism during the EDOT vapor phase polymerization process [57], leading to an inhomogeneous distribution of PEDOT within a single electrode.

The volumetric capacitance is a measure of the capacity to uptake ions in the CP film as a function of voltage. Researchers have determined the volumetric capacitance of pure PEDOT and PEDOT:PSS thin films [41, 58]. In this work, to determine the volumetric capacitance of the PEDOT electrodes, a cyclic voltammetry experiment with a three electrodes setup was employed (refer to Fig. SII2a in supplementary information). The dimensions of the trilayer are *length* (L) \times *width* (b) \times *total thickness* (h) = 5 mm \times 1 mm \times 0.017 mm in swollen state, and the thickness of each layer is $h_P = 3.5 \mu\text{m}$ and $h_S = 10 \mu\text{m}$. Madden *et al.* [23, 59] have demonstrated a variation in the volumetric capacitance value of the polypyrrole as a function of applied voltage. Since the trilayer structure works as an actuator, a variation in the applied voltage is

expected. During this experiment, the potential window was varied from 0.5 V_{pp} to 3.3 V_{pp} as depicted in Fig. 10.

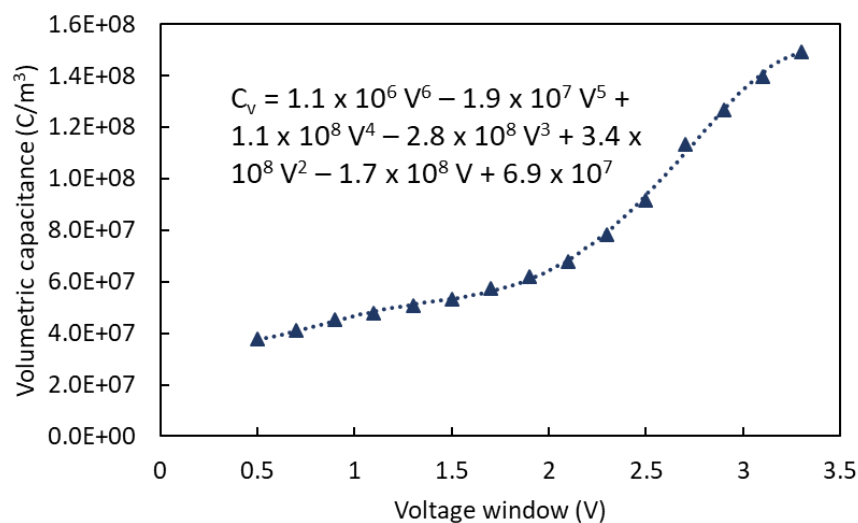


Fig. 10. Volumetric capacitance as a function of the voltage window

As can be seen in Fig. 10, the volumetric capacitance increases linearly when the potential window increases from 0.5 V_{pp} to 2.2 V_{pp}. One way of picturing this enlargement is, as the voltage increases, more and more holes or electrons are created in or supplied to the PEDOT backbone chain leading to a gain in the number of ions inserted or extracted. This increment approaches a state of complete oxidation (or reduction) state as the voltage window reaches to 2.2 V_{pp}. When this potential continues to increase, irreversible degradation occurs, which is attributed to nucleophilic attack on the polymer from the electrolyte ions [60]. In summary, the dependence of the volumetric capacitance on the potential window is approximated by the following sixth-order function:

$$C_v = 1.1 \times 10^6 V^6 - 1.9 \times 10^7 V^5 + 1.1 \times 10^8 V^4 - 2.8 \times 10^8 V^3 + 3.4 \times 10^8 V^2 - 1.7 \times 10^8 V + 6.9 \times 10^7 \text{ (F/m}^3\text{)}. \quad (17)$$

To our knowledge, the voltage dependence of the specific capacitance of PEDOT material has not been reported yet. However, this voltage dependence of other supercapacitor materials such as manganese oxide/activated carbon in 2 mol/L KNO₃ electrolyte has already been studied [61] showing an increase in the capacitance as the operating voltage increases. Equation (17) is to some extent agreed with the trend observed by Stoller [61].

3.2 Mechanical properties

The Young's moduli of the PEDOT electrodes and of the SPE layer are the importance parameters affecting the deflection output since they directly proportion to the output moment,

shown in equation (5). In this section, the Young's moduli of the SPE layer alone and of the trilayer actuator as a function of the oxidation state, were measured in a swollen state.

A specimen of the SPE layer with the following dimensions of *length* (L) \times *width* (b) \times *thickness* (h_s) = $10\text{ mm} \times 6\text{ mm} \times 0.07\text{ mm}$ was tested using a Bose Electroforce 3000 dynamic mechanical analyzer. The relationship between the force F and the displacement ΔL gives a Young's modulus E_{SPE} for the SPE material of $E_{SPE} = \frac{F}{\Delta L} \frac{L}{bh_s} = 329 \pm 50\text{ kPa}$. This value is consistent with the value reported by Festin [62] and Woehling [63] for the same type of material.

It must be recalled that Bahrami-Samani and Spinks [33, 64] have shown changes in shear modulus of a polypyrrole thin films at various applied potentials, whereas Farajollahi [32] also demonstrated the dependence of the Young's modulus of a penetrated PEDOT layer on the applied voltage. Consequently, we have decided to measure the variation of the Young's modulus of trilayer actuators versus the applied voltage. The trilayer actuator (*length* (L) \times *width* (b) \times *thickness* (h_t) = $10\text{ mm} \times 6\text{ mm} \times 0.017\text{ mm}$) was subjected a Bose Electroforce 3000 dynamic mechanical analyzer and a potentiostat (refer to Fig. SII3 in supplementary information). The Young's moduli of the trilayer actuators are described in Fig. 11.

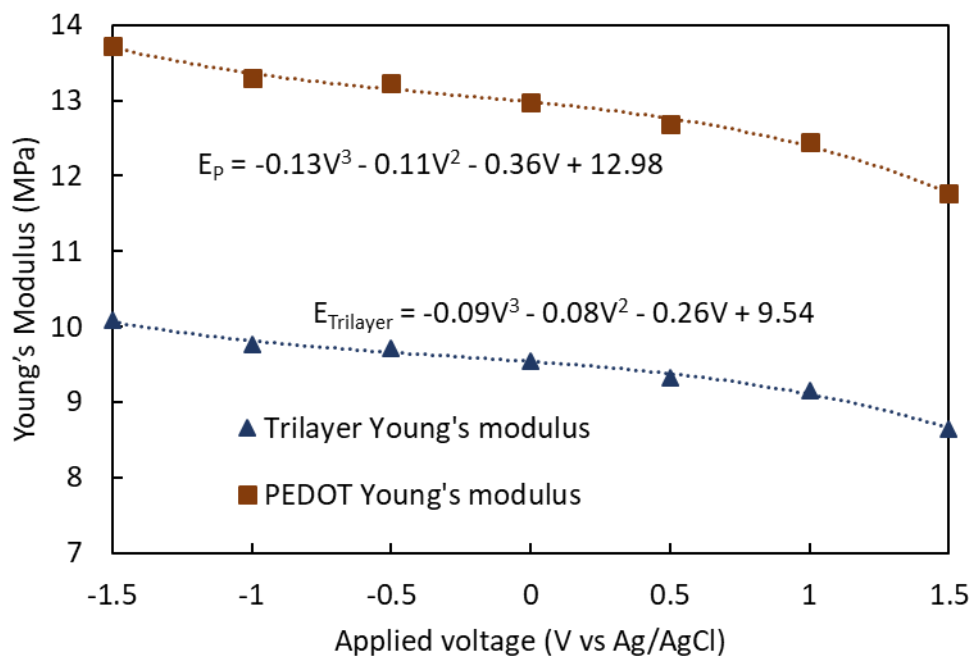


Fig. 11. Young's modulus of the trilayer actuator and the PEDOT layer as a function of applied voltage.

From the SPE Young's modulus and the trilayer Young's modulus, the Young's modulus of the PEDOT electrodes can be derived from the following equation [35] $E_P = \frac{(EI - E_S I_S)}{2I_P}$ (I_S and I_P are the moment of inertia of the SPE and the PEDOT layers' cross section, respectively) and

plotted on the same graph in Fig. 11. As we can see, the Young's modulus of both the trilayer and the PEDOT layer decreases slightly by 14 % from 10 MPa to 8.6 MPa and from 13.7 MPa to 11.7 MPa, respectively, when they are switched from reduced state (- 1.5 V) to oxidized state (1.5 V). This percentage reduction is quite consistent with the value reported by Farajollahi [32].

3.3 Coupling parameter

The coupling effect between strain and charge was first proposed by Baughman *et al.* [65] to describe the change in polyacetylene thin film length corresponding to the insertion of ions. Della Santa [37] and Madden [23] suggest a strain-to-charge ratio on the order of $10^{-10} \text{ m}^3/\text{C}$ for a polypyrrole-based CP actuator. In this work, we have figured out the strain-to-charge ratio of a PEDOT-based actuator. The proposed experimental setup was to apply a voltage to the trilayer actuator and then to record the output current and the bending response (refer to Fig. SII2c in supplementary information).

From the actuator bending data, the bending strain (Fig. 12) can be derived via the following equation $\varepsilon_{actual}(t)\% = \frac{h_t}{2} \left(\frac{1}{r_t(t)} - \frac{1}{r_0} \right)$, where r_0 and r_t are the radius of the actuator in neutral and stimulated state, respectively, and h_t is the thickness of the trilayer actuator.

From this bending strain, the active strain of the PEDOT electrodes is derived as following equation [66]:

$$\varepsilon_{active}(t) = \varepsilon_{actual}(t) \times \frac{h_p(h^4 E^2 + 8h^3 E + 12h^2 E + 8hE + 24h + 12E^2 + 20)}{6h_t(h+1)(hE+2)} = 1.61 \times \varepsilon_{actual}(t),$$

where $h = \frac{h_S}{h_P}$ and $E = \frac{E_S}{E_P}$. An error bar of 5 % obtained from the bending strain measurements has been added.

Moreover, the volumetric charge density ($\Delta Q(t)/V$, V is the one PEDOT electrode volume) (Fig. 12) resulting from the total insertion or extraction of ions per volume is calculated by integrating the current over time.

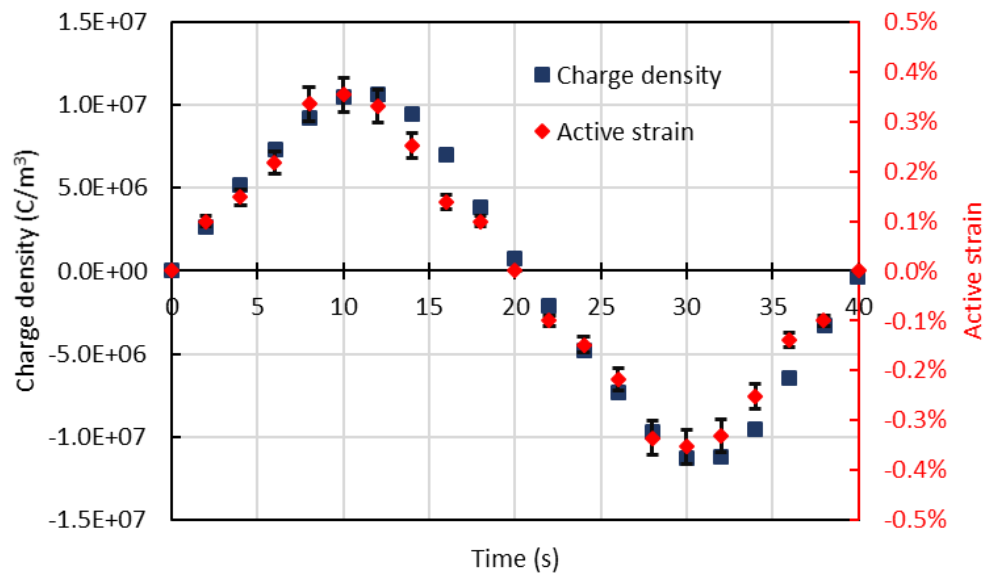


Fig. 12. Charge density and strain of the trilayer actuator as a function of time under a triangular wave voltage excitation

The strain-to-charge ratio is finally obtained by the ratio: $\alpha = \frac{\varepsilon_{active}(t)V}{\Delta Q(t)}$. The Fig. 12 shows a quite constant ratio of the active strain to charge density giving a constant value of the strain-to-charge of $3.6 \pm 0.5 \times 10^{-10}$ (m³/C).

Table 2: Summary of measured parameters of the ultrathin trilayer actuator

| | |
|--|---|
| PEDOT electrodes electrical conductivity (S/cm) | Top PEDOT electrode: $-2.62V^3 + 2.76V^2 + 9.89V + 7.49$ Bottom PEDOT electrode: $-16.6V^3 + 1.1V^2 + 51.7V + 59.1$ |
| PEDOT electrodes ionic conductivity (S/m) | Top PEDOT electrode: 0.025 Bottom PEDOT electrode: 0.030 |
| PEDOT electrodes' volumetric capacitance (F/m ³) | $1.1 \times 10^6 V^6 - 1.9 \times 10^7 V^5 + 1.1 \times 10^8 V^4 - 2.8 \times 10^8 V^3 + 3.4 \times 10^8 V^2 - 1.7 \times 10^8 V + 6.9 \times 10^7$ |
| NBR/PEO ionic conductivity (S/m) | 0.038 |
| Strain-to-charge ratio (m ³ /C) | $\alpha = 3.6 \pm 0.5 \times 10^{-10}$ |
| NBR/PEO Young's modulus (kPa) | 329 ± 50 |
| Trilayer actuator Young's modulus (MPa) | $-0.09V^3 - 0.08V^2 - 0.26V + 9.54$ |
| PEDOT Young's modulus (MPa) | $-0.13V^3 - 0.11V^2 - 0.36V + 12.98$ |
| Damping ratio | 0.39 [22] |
| Beam density (kg/m ³) | 2000 |

Table 2 summarizes the critical electrical, electrochemical, and mechanical properties of the trilayer actuators that are used in the model described below. It must be noted that in order to

1 use of the potential-dependent equations in Table 2 in the global model in section 2.3, potential
2 sensors were added to the BG model at the input of the applied voltage and along the length of
3 the beam to detect the actual magnitude of the applied voltage. The actual input voltage (V) at
4 the beginning of each beam segment is an input parameter in these voltage dependent equations
5 and the actual values can be determined. These obtained values allow the evaluation of the non-
6 linear dynamic model established and will be discussed in the next section.
7
8
9

10 11 **4. Results and discussion**

12
13
14 In the previous section, a BG model was proposed to predict actuation behavior and the
15 parameters required for the proposed model were determined. To evaluate the agreement
16 between the BG model and the experimental results, a set of experiments were performed. The
17 geometry of the trilayer actuator used in these characterizations is equal to *length \times width \times*
18 *thickness = 5 mm \times 1 mm \times 0.017 mm*, unless stated otherwise. First, the simulation and
19 experimental current outputs are compared. The proposed model also highlights a drop in
20 voltage dropped along the length of the actuator. The actuation strain, of which the magnitude
21 and frequency vary with the square of the voltage, confirms the concordance between the results
22 of the simulations and the experiments. The distinguished properties of the proposed model that
23 are different from other models [31, 32, 34] such as the integration of the mass of the actuator
24 and the inertial effect, are described. The analysis of the critical parameters affecting actuator
25 performance and the investigation of energy transmission and efficiency highlight the
26 advantages of BG representations.
27
28
29
30
31
32
33
34
35

36 **4.1 Voltage and frequency response of the actuator**

37
38
39 Fig. 13 shows a trilayer actuator under a square wave voltage excitation. An asymmetry between
40 the top and the bottom PEDOT electrode layers is from the initially curved beam state (Fig.
41 13b). The beam deflects leftwards when -1.1 V is applied to the left side (bottom) and 1.1 V is
42 applied to the top PEDOT electrode layer (Fig. 13a). As the voltage direction is reversed, the
43 beam bends back until it is straight (Fig. 13c). This curved state is due to stresses inside the
44 trilayer. The model is used to predict the relative change in curvature, which is added to the
45 experimentally observed initial curvature.
46
47
48
49
50
51
52
53
54
55
56
57
58
59
60

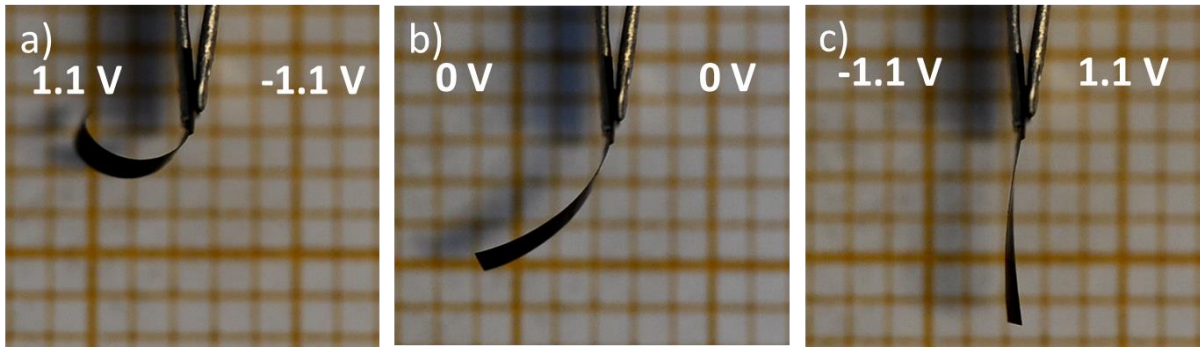


Fig. 13. Trilayer actuator under voltage excitation: a) Top PEDOT electrode voltage: -1.1 V, Bottom PEDOT electrode: 1.1 V, b) neutral state, c) Top PEDOT electrode: 1.1 V, Bottom PEDOT electrode: -1.1 V. The grid has a 1 mm spacing.

As demonstrated in the previous section, the PEDOT electrical conductivity, the PEDOT volumetric capacitance, and the Young's modulus of the trilayer actuator are dependent on the applied potential. All voltage dependencies were incorporated into the proposed BG model. These dependencies have been fitted with a polynomial to increase the rate of convergence of the BG model.

In order to characterize the electrical and electromechanical responses, a triangular wave was applied, followed by a square wave voltage driving a fast actuation response was applied to the trilayer actuator (Fig. 14a). The resulting recorded current was then compared with the output current from the electrical model.

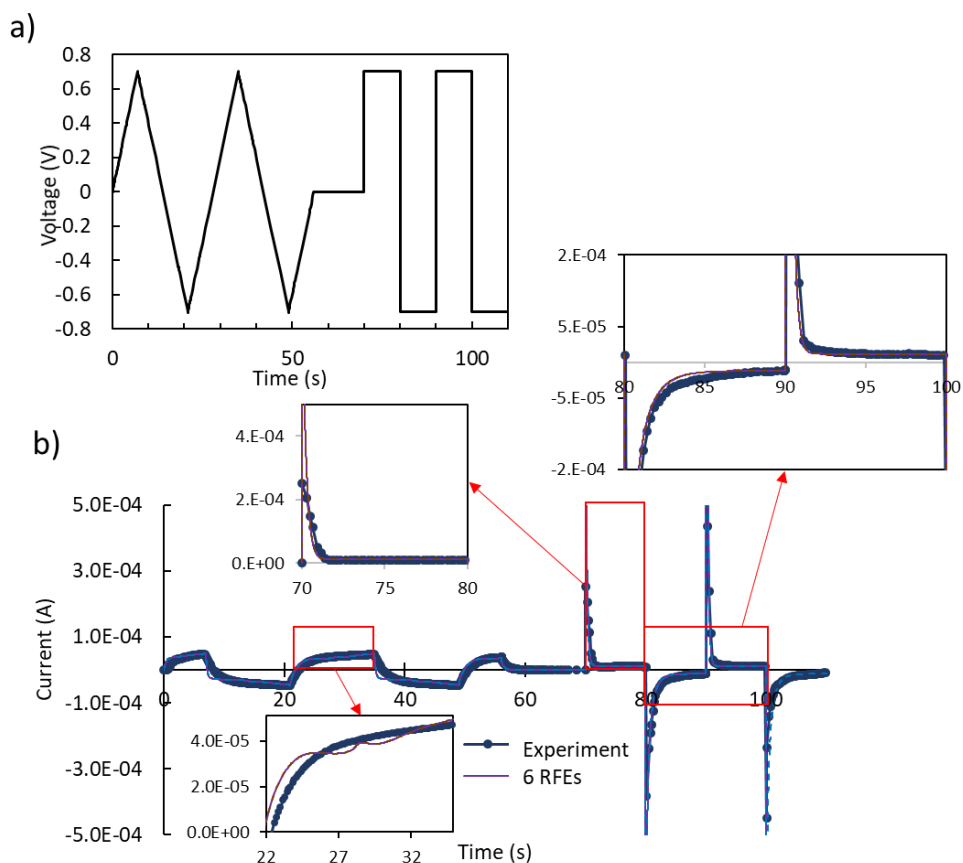


Fig. 14. a) Triangular wave and rectangular wave applied voltage, b) Measured and simulation current response

As shown in Fig. 14b, the simulated current (4 RFEs and 6 RFEs simulated current are indistinguishable, so only 6 RFEs is plotted) matched the experimental results quite well, and there is an asymmetrical in the output current between two halves cycles of the applied voltage. This asymmetry is due to the dependence of the electronic conductivity and the volumetric capacitance of the PEDOT electrodes on the applied potential. In the case of a step voltage, the response time and the amplitude of the current of the models were slightly faster than in the experiment. This is due to the limited sampling rate (5 points/s) of the device used to measure the current.

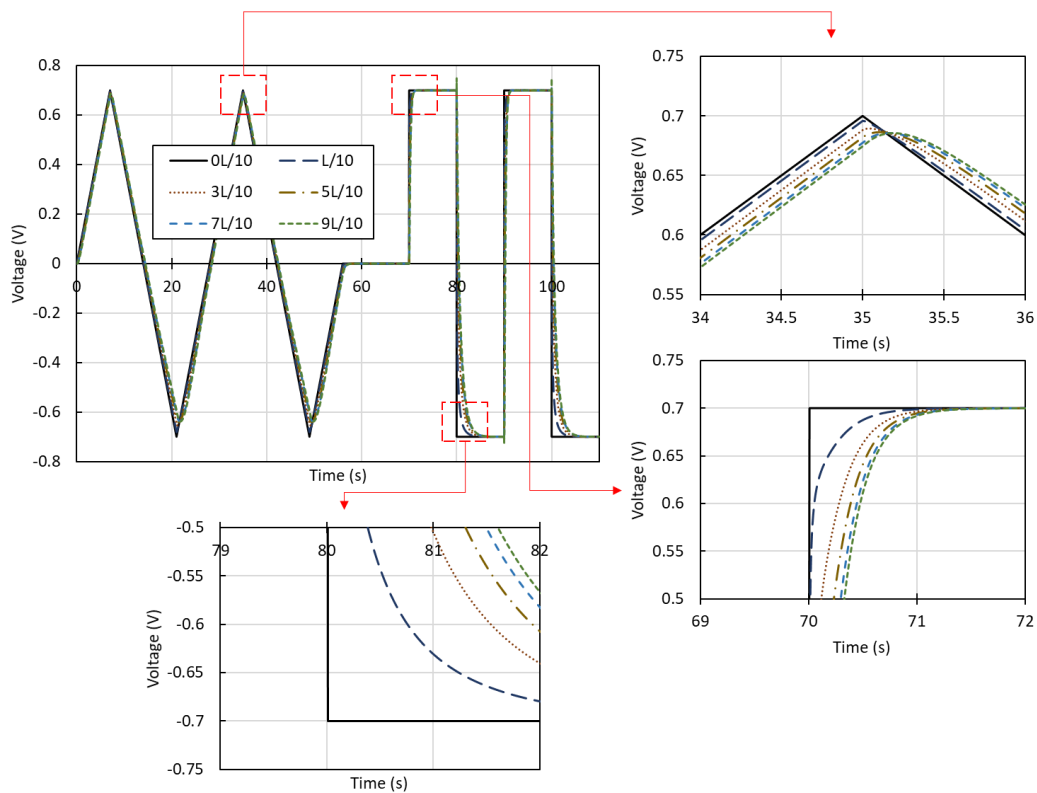


Fig. 15. Modeled voltage drops along the length of the beam due to the existence of electrical resistance of PEDOT electrodes. The legend indicates the plotting of local voltage drop as a function of distance along the trilayer from the electrical contact point, from zero (black line) to 90% of the length (fine black dash).

Fig. 15 depicts the modeled drop in voltage along the length of the beam. In the step response, a significant reduction in the voltage is observed at the position $x = L/10$ in comparison with the applied voltage (at the position $x = 0$), close to the clamping point, at short times (< 0.3 s). For longer times ($>$ than half a seconds), the drop becomes negligible. The drop increases further away from the clamping point, as expected. However, in the ramp response, it is clear that the reduction in voltage is not significant (around 7% at the tip of the beam), and the maximum voltages are shifted to the right showing a delay or a slower actuation response as we go further away from the clamping point. An asymmetric voltage between the two halves cycles of the applied voltage is also observed, which is due to the variation in PEDOT electronic conductivity following the change in voltage.

To evaluate the ability of the model to track the mechanical behavior of the trilayer actuator, the beam displacement was recorded using a camera to determine the radius of curvature and the bending strain as a function of time and position along the length of the beam. The theoretical strain was determined from the radius of curvature, which is calculated from the rotation angle θ_i of each RFE. In the first set of experiments, the magnitude of the square wave voltage was varied from 0.5 Vpp to 3 Vpp, while the frequency was held at 0.1 Hz. Fig. 16a shows quite good agreement between the measured and the theoretical strain in both cases

(where the beam was divided into 4 RFEs (3 SDEs) or 6 RFEs (5 SDEs)), except for the point where the voltage is 3 Vpp. This difference is due to a change in the electrical and the mechanical properties of the trilayer actuator as a result of the irreversible degradation in polymer chains inside the electrodes [60]. However, this change was not considered in the proposed model. Continuously operating the actuator at this high voltage will significantly decrease its lifetime. As it has been observed by the authors, after tens of cycles of deflection at this high applied voltage, the magnitude of displacement will quickly decrease to zero.

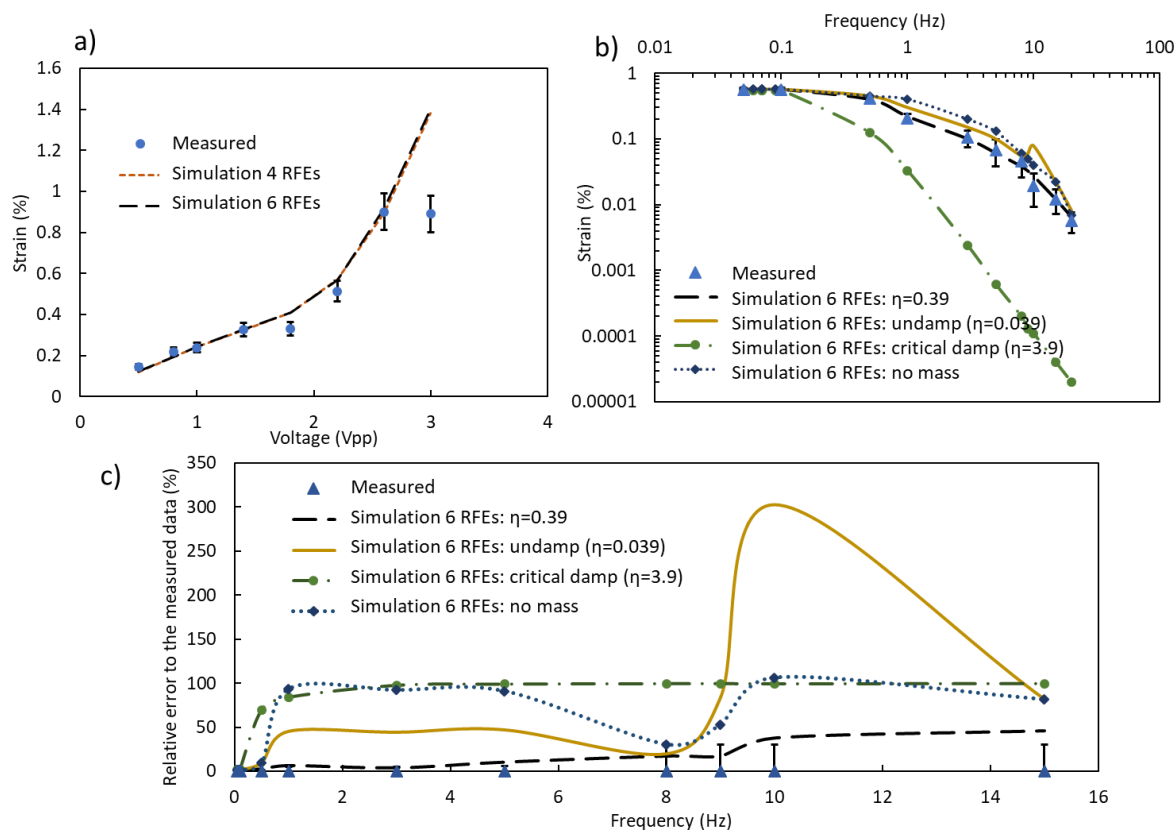


Fig. 16. Comparison between the simulations and the experiments on a) The strain as a function of the magnitude of applied voltage at a constant frequency of 0.1 Hz, b) The strain as a function of the frequency of applied voltage at a constant magnitude of ± 1.1 V, c) The relative error of the simulations compared to the measured data.

In the second set of experiments, the frequency of the applied square wave voltage was varied between 0.05 Hz and 15 Hz while the magnitude was constant at 2.2 Vpp (Fig. 16b). Fig. 16c shows the magnitude of the error between the model and the simulation as a function of frequency. To simplify these two figures, the 4 RFEs curves have been removed from the graph as it is very similar to the 6 RFEs curves, though a small difference is observed. Once again, a good agreement between the simulations (indicated by “Simulation 6 RFEs: $\eta = 0.39$ ” curve in Fig. 16b, c) and experiments is observed. It is worth noting that this damping ratio $\eta = 0.39$ was obtained via a vibration measurement [22]. However, when the frequency increases to over 5 Hz, a small difference can be seen (a relative error of approximately 15%). This inaccuracy may

come from the method used to measure the strain based on capturing actuation (limited frame rate: 24fps) and imaging analysis which is not high accuracy at high frequency.

Another advantage of the proposed model is the ability to incorporate the damping coefficient and the mass of the actuator. Damping shows a significant effect on the strain of the actuator at intermediate and high frequency (> 0.5 Hz). In the case of overdamped, where the assumed damping ratio ($\eta = 3.9$) is ten times higher than the measured value [22], the strain drastically drops as the frequency is increased and the relative error is around 100%. A small increase in strain is seen when the damping ratio is assigned as a nearly undamped ($\eta = 0.039$) situation, and the first resonant frequency of the actuator is clearly visible in this case as there is an increase in strain around 10 Hz (Fig. 16b, c). When mass of the actuator is removed from the model, there is a clear overestimation of strain by the simulation (by approximately 100%), demonstrating the importance of including mass in the simulations at moderate to high frequencies.

The model has the ability to predict the dynamic mechanical response of the beam. A voltage of 2.2 V_{pp} at 0.1 Hz was applied to the trilayer. The beam was previously hold at the position described in Fig. 13c. At the time 0 s, the voltage reserved the direction (Fig. 13a) and the dynamic behavior of the beam was captured at time steps of 0 s, 1 s, 3 s, and 5 s, and then compared to the simulation results. As shown in Fig. 17, the predicted results follow the beam movement at those time points.

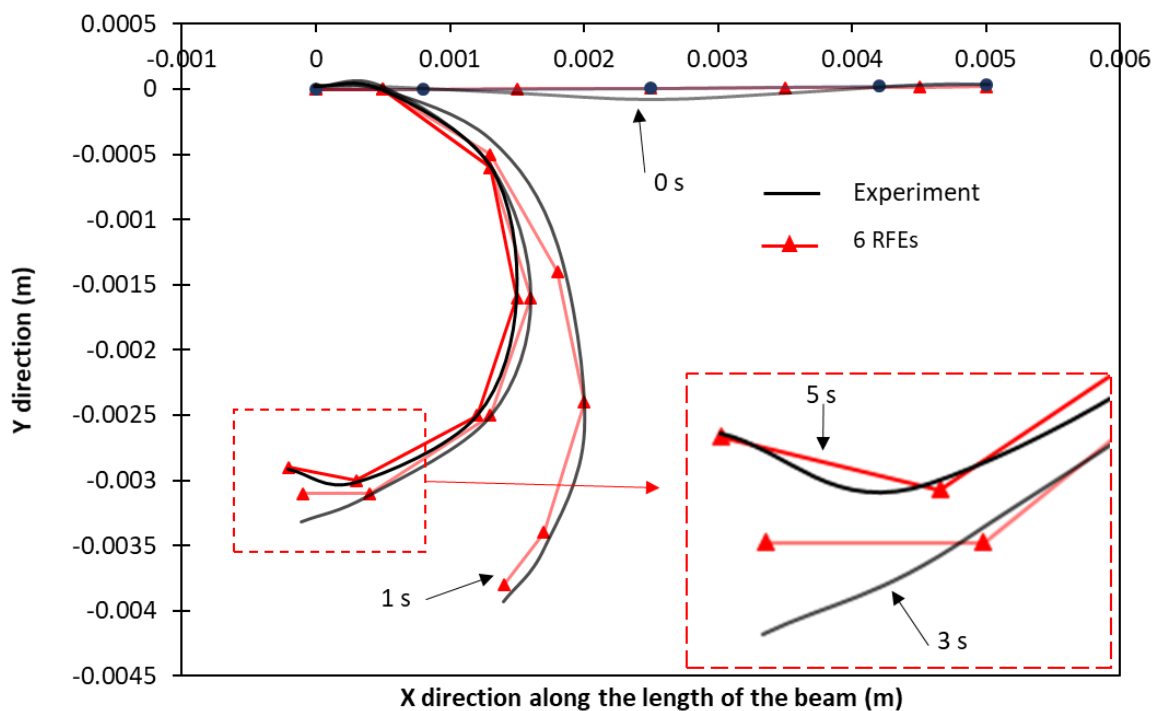


Fig. 17. Comparison between the experiment and the simulation in terms of the dynamic mechanical behavior of the beam subjected to a voltage excitation of 2.2 V_{pp} at 0.1 Hz.

In general, the non-linear model shows a good agreement with the experimental results. In comparison with previous studies, the biggest advantage of our proposed model is the ability to implement the non-linear behavior of the PEDOT electrical conductivity and volumetric capacitance and the Young's modulus of the trilayer actuator due to its dependence on the oxidation state. The integration of the mass and damping effect into the proposed model allows prediction of the actuation behavior at high frequency – which has become important as high actuation rates are reached [19]. The ability to extract the non-linear dynamic mechanical displacement of the beam is another benefit of the model, which allows us to track beam motion as a function of time. In addition, the model can also provide an insight into actuator performance as a function of its critical parameters, which have been characterized. For example, Fig. 18 gives an assessment of how sensitive the active strain difference is to Young's modulus, PEDOT electrical conductivity, SPE ionic conductivity, and the length of the actuator at both low (Fig. 18a) and high frequency (Fig. 18b). This result suggests that for the actuator geometry studied, reducing elastic modulus will have a significant effect on deflection, while the influence of the length depends on the frequency. Not surprisingly, conductivity has little effect on strain at low frequencies of operation, but this effect becomes large at high frequencies.

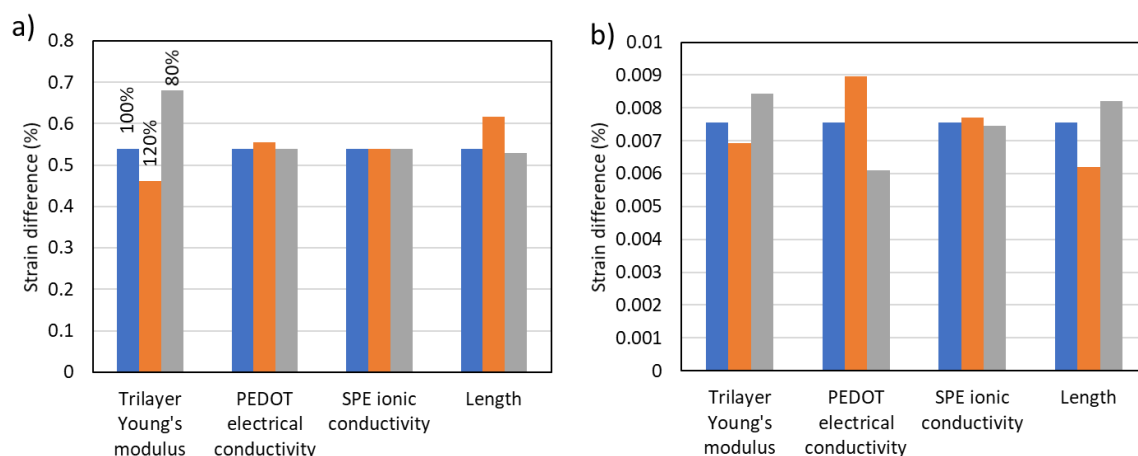


Fig. 18. Key factors affecting the actuator displacement under a square wave voltage ($V_{pp} = 2.4$ V), a) at low frequency $f = 0.1$ Hz, and b) at high frequency $f = 20$ Hz. For each parameter, three columns from left to right represent for its real value (blue column), its value increased by 20% (orange column), and its value reduced by 20% (gray column).

The values of these parameters have been adjusted by $\pm 20\%$ of their values while the others were maintained constant. It is clear that at low frequency ($f = 0.1$ Hz) of an applied voltage, an increase of the PEDOT electrical conductivity would lead to an increase in strain difference while a stiffer beam would reduce its displacement. SPE ionic conductivity shows a small effect on the beam displacement, as expected. At high frequency ($f = 20$ Hz), while the effect of the

Young's modulus remains similar, the PEDOT conductivity and ionic conductivity have a great influence on the strain difference, and the outcome of changing length of the actuator is reversed.

4.2 Power and efficiency study

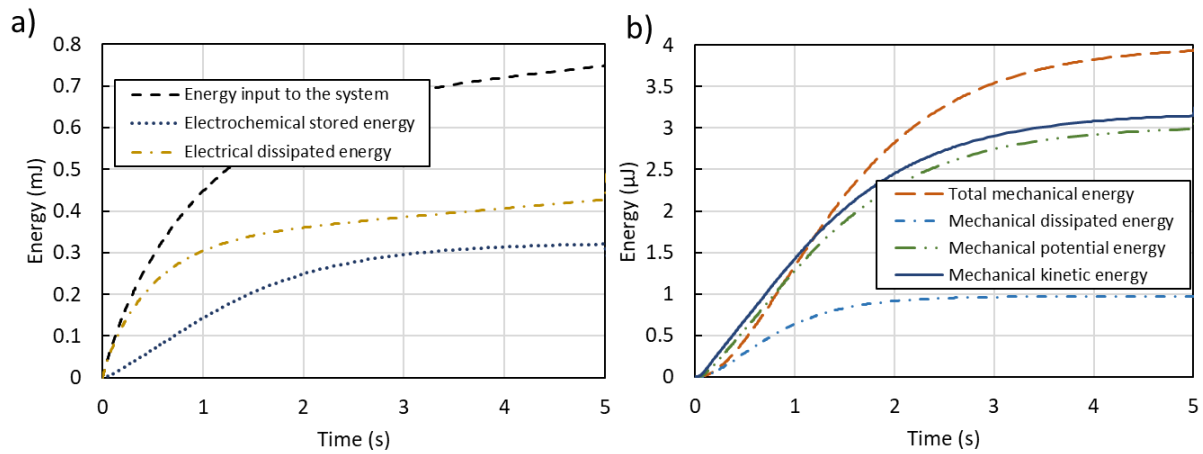


Fig. 19. Evolution of energy over half a period of applied voltage: a) The electrochemical energy, and b) The mechanical energy.

One advantage of the BG models is that they allow ready access to information about the energy stored, dissipated, and transmitted – in this case electrochemical and mechanical energies. Considering half a period of the applied voltage (0.1 Hz at 2 Vpp), Fig. 19 shows the evolution of the electrical (left) and the much smaller mechanical (right) components energies with time, including both stored and dissipated contributions. As expected for a system composed of resistors with capacitors in series, the input energy increases with time until the energy storage is complete (Fig. 19a). Mechanical energy also rises and then saturates, with the same time constant (Fig. 19b). Fig. 20 replots the stored and dissipated energy components of energy as fractions of the total input energy. From this plot it is evident that the mechanical energy represents about 0.5% of the total. 40 % of the input electrical energy is stored, which is not surprising since a 50:50 split is what would be expected from a simple series RC circuit that is charged with a step voltage input. A slow ramp input, in which currents are kept small to minimize IR drop, would lead to a significantly higher component of stored energy. On the mechanical side, kinetic energy rises quickly and then decays again as the actuator accelerates and then decelerates. Dissipation loss, which depends on speed, also rises quickly, and then reaches saturation, as the trilayer comes to a stop. The stored mechanical energy is elastic potential energy that accumulates as the beam bends, and is about 55% of the total. Dissipation losses can be reduced, once again, by actuating slower. The relatively small fraction of electrical energy converted to mechanical is consistent with previous reports showing a small electromechanical coupling coefficient [23, 67, 68]. The efficiency however need not be so small, especially in slow charging situations where much of the input electrical energy can be

recovered during discharge. Previous work shows that that overall efficiency can exceed 10 %, if electrical energy is recovered [23].

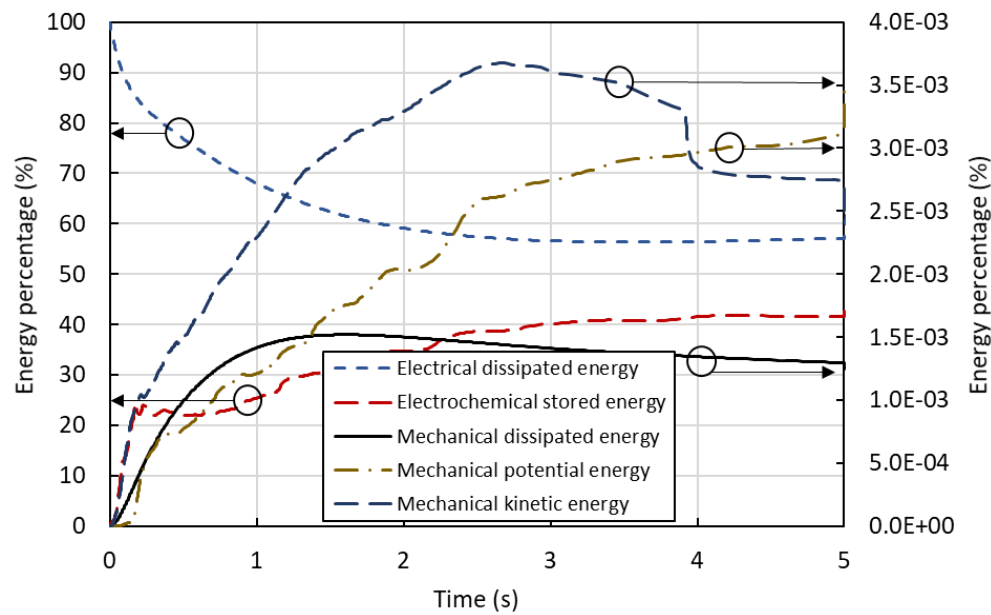


Fig. 20. Instantaneous electrical to mechanical coupling.

5. Conclusion

In this paper, a non-linear dynamic model has been proposed to simulate the actuation of an ultrathin trilayer actuators developed using a new fabrication process. The model showed advances to the existing work on trilayer actuator in that it can precisely predict a non-linear dynamic actuation with an ability to implement non-linear electrochemical and mechanical properties of material: PEDOT electrical and ionic conductivities; volumetric capacitance values; and Young's modulus variation. In addition, it accounted for the mass and damping associated with the beam. All physical characteristics used in the model were measured. The approach is represented in bond graph language, providing simple way to access the energy information and evaluate the critical operational parameters of the actuator.

In general, the model enables us to predict non-linear dynamic behavior, allows an insight into the phenomena occurring in the ionic actuator, and an access to the energy information. The model is believed to be a useful tool for the ionic trilayer actuator design process.

Acknowledgments

This project received funding from the European Union's Horizon 2020 research and innovation program under Marie Skłodowska-Curie grant agreement No 641822 - MICACT. This work was partly supported by the French Government through the National Research Agency (ANR)

1 under program PIA EQUIPEX LEAF (ANR-11-EQPX-0025), RENATECH and MICRO-TIP
2 projects.
3

4 **References**

- 5
6
7 [1] A. Maziz, A. Concas, A. Khaldi, J. Stålhand, N.-K. Persson, E.W.H. Jager, Knitting and
8 weaving artificial muscles, *Science Advances*, 3(2017).
9 [2] M.Y. Coskun, C. Sancak, M. Itik, G. Alici, Hybrid force and position control of a conducting
10 tri-layer electro-active polymer actuator, *Transactions of the Institute of Measurement and*
11 *Control*, 39(2016) 288-96.
12 [3] T. Götttsche, S. Haeberle, *Integrated Oral Drug Delivery System with Valve Based on*
13 *Polypyrrole, Biomedical Applications of Electroactive Polymer Actuators*, John Wiley & Sons,
14 Ltd2009, pp. 301-16.
15 [4] E.W. Jager, Immerstrand, C., Peterson, K.H. et al. , *The Cell Clinic: Closable Microvials*
16 *for Single Cell Studies, Biomedical Microdevices*, 4(2002) 10.
17 [5] W.H.J. Edwin, Ingan, xe, O. s, Lundstr, xf, et al., *Microrobots for Micrometer-Size Objects*
18 *in Aqueous Media: Potential Tools for Single-Cell Manipulation, Science*, 288(2000) 2335-8.
19 [6] A. Della Santa, A. Mazzoldi, D. De Rossi, *Steerable microcatheters actuated by embedded*
20 *conducting polymer structures, Journal of Intelligent Material Systems and Structures*, 7(1996)
21 292-300.
22 [7] Y. Naka, M. Fuchiwaki, K. Tanaka, *A micropump driven by a polypyrrole-based conducting*
23 *polymer soft actuator, Polymer International*, 59(2010) 352-6.
24 [8] Y. Fang, X. Tan, *A novel diaphragm micropump actuated by conjugated polymer petals:*
25 *Fabrication, modeling, and experimental results, Sensors and Actuators A: Physical*, 158(2010)
26 121-31.
27 [9] K. Ikushima, S. John, A. Ono, S. Nagamitsu, *PEDOT/PSS bending actuators for autofocus*
28 *micro lens applications, Synthetic Metals*, 160(2010) 1877-83.
29 [10] S.A. Wilson, R.P.J. Jourdain, Q. Zhang, R.A. Dorey, C.R. Bowen, M. Willander, et al.,
30 *New materials for micro-scale sensors and actuators. An engineering review, Materials Science*
31 *and Engineering R: Reports*, 56(2007) 1-129.
32 [11] D. Pede, E. Smela, T. Johansson, M. Johansson, O. Inganäs, *A general-purpose conjugated-*
33 *polymer device array for imaging, Advanced Materials*, 10(1998) 233-7.
34 [12] R. Kiefer, X. Mandviwalla, R. Archer, S.S. Tjahyono, H. Wang, B. MacDonald, et al., *The*
35 *application of polypyrrole trilayer actuators in microfluidics and robotics, Proceedings of SPIE*
36 *- The International Society for Optical Engineering2008*.
37 [13] E.W.H. Jager, N. Masurkar, N.F. Nworah, B. Gaihre, G. Alici, G.M. Spinks, *Patterning*
38 *and electrical interfacing of individually controllable conducting polymer microactuators,*
39 *Sensors and Actuators B: Chemical*, 183(2013) 283-9.
40 [14] A. Khaldi, D. Falk, K. Bengtsson, A. Maziz, D. Filippini, N.D. Robinson, et al., *Patterning*
41 *highly conducting conjugated polymer electrodes for soft and flexible microelectrochemical*
42 *devices, ACS Applied Materials & Interfaces*, (2018).
43 [15] C.A. Cutler, M. Bouguettaya, J.R. Reynolds, *PEDOT polyelectrolyte based electrochromic*
44 *films via electrostatic adsorption, Advanced Materials*, 14(2002) 684-8.
45 [16] A. Mazzoldi, A.D. Santa, D. De Rossi, *Conducting Polymer Actuators: Properties and*
46 *Modeling*, in: Y. Osada, D.E. De Rossi (Eds.), *Polymer Sensors and Actuators*, Springer Berlin
47 Heidelberg, Berlin, Heidelberg, 2000, pp. 207-44.
48 [17] E. Smela, *Conjugated Polymer Actuators for Biomedical Applications, Advanced*
49 *Materials*, 15(2003) 481-94.
50 [18] A. Khaldi, C. Plesse, C. Soyer, E. Cattan, F. Vidal, C. Legrand, et al., *Conducting*
51 *interpenetrating polymer network sized to fabricate microactuators, Applied Physics Letters*,
52 98(2011).
53
54
55
56
57
58
59
60

- 1 [19] A. Maziz, C. Plesse, C. Soyer, C. Chevrot, D. Teyssié, E. Cattan, et al., Demonstrating kHz
2 Frequency Actuation for Conducting Polymer Microactuators, *Advanced Functional Materials*,
3 24(2014) 4851-9.
- 4 [20] S.W. John, G. Alici, C.D. Cook, Validation of Resonant Frequency Model for Polypyrrole
5 Trilayer Actuators, *IEEE/ASME Transactions on Mechatronics*, 13(2008) 401-9.
- 6 [21] A. Maziz, C. Plesse, C. Soyer, E. Cattan, F. Vidal, Top-down Approach for the Direct
7 Synthesis, Patterning, and Operation of Artificial Micromuscles on Flexible Substrates, *ACS*
8 *Appl Mater Interfaces*, 8(2016) 1559-64.
- 9 [22] N.T. Nguyen, C. Plesse, F. Vidal, C. Soyer, S. Grondel, J.D.W. Madden, et al.,
10 Microfabricated PEDOT trilayer actuators: synthesis, characterization, and modeling, *SPIE*
11 *Smart Structures and Materials + Nondestructive Evaluation and Health Monitoring, SPIE2017*,
12 p. 13.
- 13 [23] J.D.W. Madden, *Conducting polymer actuators: Massachusetts Institute of Technology;*
14 2000.
- 15 [24] T. Shoa, J.D. Madden, N.R. Munce, V. Yang, Analytical modeling of a conducting
16 polymer-driven catheter, *Polymer International*, 59(2010) 343-51.
- 17 [25] G. Alici, B. Mui, C. Cook, Bending modeling and its experimental verification for
18 conducting polymer actuators dedicated to manipulation applications, *Sensors and Actuators*,
19 *A: Physical*, 126(2006) 396-404.
- 20 [26] D. Karnopp, *System dynamics : modeling and simulation of mechatronic systems*,
21 *Hoboken: Wiley;* 2012.
- 22 [27] M. Szczotka, A modification of the rigid finite element method and its application to the
23 J-lay problem, *Acta Mechanica*, 220(2011) 183-98.
- 24 [28] G. Nishida, K. Takagi, B. Maschke, T. Osada, Multi-scale distributed parameter modeling
25 of ionic polymer-metal composite soft actuator, *Control Engineering Practice*, 19(2011) 321-
26 34.
- 27 [29] B.J. Yi, I. Busch-Vishniac, Modeling of EAPs as multiple energy domain systems: A bond
28 graph approach, *Proceedings of SPIE - The International Society for Optical Engineering2006*.
- 29 [30] T.A. Bowers, MSc thesis title: Modeling, Simulation, and Control of a Polypyrrole-Based
30 Conducting Polymer Actuator: Massachusetts Institute of Technology; 2004.
- 31 [31] M. Bentefrit, S. Grondel, C. Soyer, A. Fannir, E. Cattan, J.D. Madden, et al., Linear finite-
32 difference bond graph model of an ionic polymer actuator, *Smart Materials and Structures*,
33 26(2017) 095055.
- 34 [32] F. Meisam, S. Farrokh, N. Naser, F. Adelyne, P. Cédric, T.M.N. Giao, et al.,
35 Characterization and dynamic charge dependent modeling of conducting polymer trilayer
36 bending, *Smart Materials and Structures*, 25(2016) 115044.
- 37 [33] G.M. Spinks, L. Liu, G.G. Wallace, D. Zhou, Strain Response from Polypyrrole Actuators
38 under Load, *Advanced Functional Materials*, 12(2002) 437-40.
- 39 [34] C.H. Nguyen, G. Alici, G.G. Wallace, Modelling trilayer conjugated polymer actuators for
40 their sensorless position control, *Sensors and Actuators A: Physical*, 185(2012) 82-91.
- 41 [35] G. Alici, B. Mui, C. Cook, Bending modeling and its experimental verification for
42 conducting polymer actuators dedicated to manipulation applications, *Sensors and Actuators A:*
43 *Physical*, 126(2006) 396-404.
- 44 [36] C.H. Nguyen, G. Alici, G.G. Wallace, Modelling trilayer conjugated polymer actuators for
45 their sensorless position control, *Sensors and Actuators, A: Physical*, 185(2012) 82-91.
- 46 [37] A.D. Santa, D.D. Rossi, A. Mazzoldi, Characterization and modelling of a conducting
47 polymer muscle-like linear actuator, *Smart Materials and Structures*, 6(1997) 23.
- 48 [38] T.N. Nguyen, K. Rohtlaid, C. Plesse, G.T.M. Nguyen, C. Soyer, S. Grondel, et al., Ultrathin
49 electrochemically driven conducting polymer actuators: fabrication and
50 electrochemomechanical characterization, *Electrochimica Acta*, 265(2018) 670-80.
- 51 [39] G.A. Snook, P. Kao, A.S. Best, Conducting-polymer-based supercapacitor devices and
52 electrodes, *Journal of Power Sources*, 196(2011) 1-12.
- 53
54
55
56
57
58
59
60

- 1 [40] F. Vidal, C. Plesse, D. Teyssié, C. Chevrot, Long-life air working conducting semi-
2 IPN/ionic liquid based actuator, *Synthetic Metals*, 142(2004) 287-91.
- 3 [41] C.M. Proctor, J. Rivnay, G.G. Malliaras, Understanding volumetric capacitance in
4 conducting polymers, *Journal of Polymer Science Part B: Polymer Physics*, 54(2016) 1433-6.
- 5 [42] J.D. Madden, P.G. Madden, I.W. Hunter, Conducting polymer actuators as engineering
6 materials, SPIE's 9th Annual International Symposium on Smart Structures and Materials,
7 SPIE2002, p. 15.
- 8 [43] J.C.E. Marin S. Halper, Supercapacitors: A Brief Overview, MITRE Nanosystems Group,
9 2006.
- 10 [44] P.G.A. Madden, Development and Modeling of Conducting Polymer Actuators and the
11 Fabrication of a Conducting Polymer Based Feedback Loop, MASSACHUSETTS INSTITUTE
12 OF TECHNOLOGY: MASSACHUSETTS INSTITUTE OF TECHNOLOGY; 2003.
- 13 [45] J.D.W. Madden, PhD thesis title: Conducting Polymer Actuators, Massachusetts Institute
14 of Technology 2000.
- 15 [46] S.A. Sina, H.M. Navazi, H. Haddadpour, An analytical method for free vibration analysis
16 of functionally graded beams, *Materials & Design*, 30(2009) 741-7.
- 17 [47] A. Labuschagne, N.F.J. van Rensburg, A.J. van der Merwe, Comparison of linear beam
18 theories, *Mathematical and Computer Modelling*, 49(2009) 20-30.
- 19 [48] G.R. Bhashyam, G. Prathap, Galerkin finite element method for non-linear beam vibrations,
20 *Journal of Sound and Vibration*, 72(1980) 191-203.
- 21 [49] E. Wittbrodt, I. Adamiec-Wójcik, S.a. Wojciech, SpringerLink ebooks - Engineering
22 (2006), Dynamics of flexible multibody systems : rigid finite element method, Berlin: Springer;
23 2006.
- 24 [50] A.A. Shabana, Flexible Multibody Dynamics: Review of Past and Recent Developments,
25 *Multibody System Dynamics*, 1(1997) 189-222.
- 26 [51] I.A.-W. Edmund Wittbrodt, Stanislaw Wojciech, The Rigid Finite Element Method,
27 Dynamics of Flexible Multibody Systems: Rigid Finite Element Method, Springer Berlin
28 Heidelberg, Berlin, Heidelberg, 2006, pp. 35-82.
- 29 [52] S. Wojciech, I. Adamiec-Wójcik, Nonlinear vibrations of spatial viscoelastic beams, *Acta*
30 *Mechanica*, 98(1993) 15-25.
- 31 [53] Y. Dobashi, A. Fannir, M. Farajollahi, A. Mahmoudzadeh, A. Usgaocar, D. Yao, et al., Ion
32 Transport in Polymer Composites with Non-Uniform Distributions of Electronic Conductors,
33 *Electrochimica Acta*, 247(2017) 149-62.
- 34 [54] D.S. Yoo, A. Mahmoudzadeh, E.C.W. Fok, K. Walus, J.D.W. Madden, Multiple time
35 constant modelling of a printed conducting polymer electrode, *Electrochimica Acta*, 56(2011)
36 4711-6.
- 37 [55] B.J. Feldman, P. Burgmayer, R.W. Murray, The potential dependence of electrical
38 conductivity and chemical charge storage of poly(pyrrole) films on electrodes, *Journal of the*
39 *American Chemical Society*, 107(1985) 872-8.
- 40 [56] M.R. Warren, J.D. Madden, A structural, electronic and electrochemical study of
41 polypyrrole as a function of oxidation state, *Synthetic Metals*, 156(2006) 724-30.
- 42 [57] D. Evans, M. Fabretto, M. Mueller, K. Zuber, R. Short, P. Murphy, Structure-directed
43 growth of high conductivity PEDOT from liquid-like oxidant layers during vacuum vapor phase
44 polymerization, *Journal of Materials Chemistry*, 22(2012) 14889-95.
- 45 [58] N. Kurra, R. Wang, H.N. Alshareef, All conducting polymer electrodes for asymmetric
46 solid-state supercapacitors, *Journal of Materials Chemistry A*, 3(2015) 7368-74.
- 47 [59] M. Farajollahi, G. Alici, M.S. Sarwar, J.D.W. Madden, Conducting Polymers as EAPs:
48 Physical Description and Simulation, in: F. Carpi (Ed.) *Electromechanically Active Polymers:*
49 *A Concise Reference*, Springer International Publishing, Cham, 2016, pp. 353-83.
- 50 [60] J. Ding, D. Zhou, G. Spinks, G. Wallace, S. Forsyth, M. Forsyth, et al., Use of Ionic Liquids
51 as Electrolytes in Electromechanical Actuator Systems Based on Inherently Conducting
52 Polymers, *Chemistry of Materials*, 15(2003) 2392-8.
- 53
54
55
56
57
58
59
60

- 1 [61] M.D. Stoller, R.S. Ruoff, Best practice methods for determining an electrode material's
2 performance for ultracapacitors, *Energy and Environmental Science*, 3(2010) 1294-301.
- 3 [62] N. Festin, Conducting interpenetrating polymer network actuator sensor for biomimetic
4 perception system: Université de Cergy Pontoise; 2012.
- 5 [63] V. Woehling, New Developments in electroactive materials based on electronic conductive
6 polymers : Towards integration into biomedical systems: Université de Cergy Pontoise; 2016.
- 7 [64] M. Bahrami-Samani, C.D. Cook, J.D. Madden, G.M. Spinks, P.G. Whitten, Quartz crystal
8 microbalance study of volume changes and modulus shift in electrochemically switched
9 polypyrrole, *Thin Solid Films*, 516(2008) 2800-7.
- 10 [65] R.H. Baughman, L.W. Shacklette, R.L. Elsenbaumer, E.J. Plichta, C. Becht, Micro
11 Electromechanical Actuators Based on Conducting Polymers, in: P.I. Lazarev (Ed.) *Molecular*
12 *Electronics: Materials and Methods*, Springer Netherlands, Dordrecht, 1991, pp. 267-89.
- 13 [66] P. Du, X. Lin, X. Zhang, A multilayer bending model for conducting polymer actuators,
14 *Sensors and Actuators A: Physical*, 163(2010) 240-6.
- 15 [67] T. Shoa, J.D.W. Madden, T. Mirfakhrai, G. Alici, G.M. Spinks, G.G. Wallace,
16 Electromechanical coupling in polypyrrole sensors and actuators, *Sensors and Actuators, A:*
17 *Physical*, 161(2010) 127-33.
- 18 [68] J.D.W. Madden, N.A. Vandesteeg, P.A. Anquetil, P.G.A. Madden, A. Takshi, R.Z. Pytel,
19 et al., Artificial muscle technology: Physical principles and naval prospects, *IEEE Journal of*
20 *Oceanic Engineering*, 29(2004) 706-28.
- 21
22
23
24
25
26
27
28
29
30
31
32
33
34
35
36
37
38
39
40
41
42
43
44
45
46
47
48
49
50
51
52
53
54
55
56
57
58
59
60